

DRI File Copy

ESD ACCESSION LIST  
DRI Call No. 78363  
Copy No. 1 of 2 cys.

4

Solid State Research

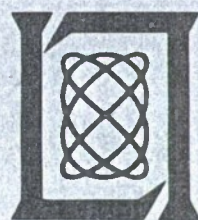
1972

Prepared for the Department of the Air Force  
under Electronic Systems Division Contract F19628-73-C-0002 by

**Lincoln Laboratory**

MASSACHUSETTS INSTITUTE OF TECHNOLOGY

LEXINGTON, MASSACHUSETTS



AD757559

ESD RECORD COPY  
RETURN TO  
SCIENTIFIC & TECHNICAL INFORMATION DIVISION  
(DRI), Building 1435

Approved for public release; distribution unlimited.

---

---

4

---

---

1972

# Solid State Research

Issued 13 February 1973

---

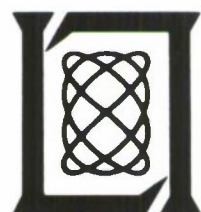
Prepared for the Department of the Air Force  
under Electronic Systems Division Contract F19628-73-C-0002 by

# Lincoln Laboratory

MASSACHUSETTS INSTITUTE OF TECHNOLOGY

LEXINGTON, MASSACHUSETTS

---



Approved for public release; distribution unlimited.

The work reported in this document was performed at Lincoln Laboratory, a center for research operated by Massachusetts Institute of Technology, with the support of the Department of the Air Force under Contract F19628-73-C-0002.

This report may be reproduced to satisfy needs of U.S. Government agencies.

Non-Lincoln Recipients

**PLEASE DO NOT RETURN**

Permission is given to destroy this document  
when it is no longer needed.

## ABSTRACT

This report covers in detail the solid state research work of the Solid State Division at Lincoln Laboratory for the period 1 August through 31 October 1972. The topics covered are Solid State Device Research, Quantum Electronics, Materials Research, Physics of Solids and Microelectronics. The Microsound work is sponsored by ABMDA and is reported under that program.

Accepted for the Air Force  
Joseph J. Whelan, USAF  
Acting Chief, Lincoln Laboratory Liaison Office

# CONTENTS

Abstract	iii
Introduction	vii
Reports on Solid State Research	x
Organization	xvi
I. SOLID STATE DEVICE RESEARCH	1
A. Field-Plate-Guarded InSb Photodiode Arrays	1
B. PbS Photodiodes Fabricated by Sb <sup>+</sup> Ion Implantation	4
C. Photodiodes Fabricated in Epitaxial PbTe by Sb <sup>+</sup> Ion Implantation	11
D. Thermal Properties of PbS <sub>1-x</sub> Se <sub>x</sub> Diode Lasers	13
1. Current-Tuning with DC and Small-Signal AC	13
2. Pulsed Operation	17
II. QUANTUM ELECTRONICS	21
A. Efficient Optically Pumped InP and In <sub>x</sub> Ga <sub>1-x</sub> As Lasers	21
B. Pressure-Tuned GaAs Diode Lasers for High-Resolution Spectroscopy	23
C. Spin-Flip Raman Linewidth Measurements and Nonlinear Processes in InSb	25
III. MATERIALS RESEARCH	31
A. Pseudobinary Phase Diagram and Existence Regions for PbS <sub>1-x</sub> Se <sub>x</sub>	31
B. Analysis of PbS <sub>1-x</sub> Se <sub>x</sub> Alloys by X-Ray Fluorescence	33
IV. PHYSICS OF SOLIDS	35
A. Rare-Earth Upconverting Phosphors	35
B. Stable, High Yield Secondary-Electron-Emitting Cathodes	36
C. Application of Free Energy Model to the High Temperature Phase Transition in Cr-Doped V <sub>2</sub> O <sub>3</sub>	41
D. Laser Spectroscopy	41
1. Zeeman Spectra of Q-Branch Absorption Lines of NO	41
2. Observation of Nuclear Hyperfine Structure in the R-Branch of NO at 77K	43
V. MICROELECTRONICS	47
A. Electron-Beam Semiconductor Diodes	47
B. IMPATT Diode Packaging Facility	52
C. Use of Molybdenum and Molybdenum-Gold Films as Metalization for Silicon Devices	52
D. Thin-Film Inductors	53
E. Thin-Film Resistor Chips	54
F. Layout and Mask Making Areas	54

# INTRODUCTION

## I. SOLID STATE DEVICE RESEARCH

Linear arrays of 20 closely-spaced InSb n-p junction photodiodes have been fabricated using the techniques of proton bombardment and field plate guarding. These arrays exhibit good elemental detector performance as well as excellent uniformity among elements of an array. The variation in the detectivity of the elements in an array was measured to be less than 10 percent. In addition, the yield of good arrays per wafer has been unusually high. Out of 50 arrays fabricated on a single wafer, only seven arrays had defective diodes.

Using Sb<sup>+</sup> ion implantation to create the n-type layer, n-p junction photodiodes in PbS have been fabricated. The Sb<sup>+</sup> implantation process is similar to that previously used in the fabrication of bulk PbTe photodiodes. The zero-bias resistance for the 15-mil-square PbS diodes was typically 200 ohms at 300°K,  $5 \times 10^4$  ohms at 195°K, and  $5 \times 10^9$  ohms at 77°K. Peak detectivities occurred at 2.55, 2.95 and 3.4 μm at 300°, 195° and 77°K, respectively. The corresponding measured detectivities were  $4.8 \times 10^9$ ,  $1.1 \times 10^{11}$  and  $4.2 \times 10^{12}$  cmHz<sup>1/2</sup>/W. The 77°K detectivity was measured in a reduced background and was amplifier noise limited. Peak quantum efficiencies were typically 50 to 60 percent.

Similar Sb<sup>+</sup> ion implants into PbTe films which have been grown epitaxially on BaF<sub>2</sub> substrates have also yielded high quality n-p photodiodes. At 77°K, a typical 15-mil-square photodiode had a zero-bias resistance of 1 megohm, a peak detectivity of  $4.5 \times 10^{11}$  cmHz<sup>1/2</sup>/W at 5.3 μm and a quantum efficiency of 55 percent.

The thermal properties of PbS<sub>1-x</sub>Se<sub>x</sub> diode lasers with n-p junctions formed by Sb<sup>+</sup> ion implantation have been studied by observing the temperature tuning of the laser frequency for a number of different operating conditions. The continuous DC tuning rate was measured as a function of current in CW operation, the thermal response was determined by applying a small-amplitude AC current to a DC-biased laser, and the laser frequency chirp rate was measured under pulsed conditions.

## II. QUANTUM ELECTRONICS

Using an optical parametric oscillator as an optical pump, peak powers of the order of one watt and conversion efficiencies of 3 to 4 percent have been obtained from InP and In<sub>x</sub>Ga<sub>1-x</sub>As semiconductor lasers. Tuning of the pump allows bulk optical excitation, thus reducing surface recombination and spreading the heat load.

Gallium arsenide diode lasers operating at 77°K have been hydrostatic pressure tuned in the 0- to 7-kbar range and their spectral characteristics have been studied. Time resolved spectroscopy has been carried out on Cs<sup>133</sup> using the frequency swept output of a pulsed laser. Sufficient resolution is obtained for Doppler-limited spectroscopy.

## Introduction

Small signal gain measurements have been made on the spin-flip Raman laser by observing the amplification of a second CO laser line at a frequency lower than the pump line. Measurements of the Raman gain profile were made by tuning the spin-flip frequency through the frequency difference between the CO laser lines. By observing the gain profile at a number of CO line separations the dependence of linewidth on magnetic field was determined. Four wave mixing processes were also seen.

## III. MATERIALS RESEARCH

The pseudobinary phase diagram of the PbS-PbSe system has been re-determined by using thermal analysis to measure the liquidus temperatures and electron microprobe analysis of Bridgman-grown ingots to establish the solidus points. The chalcogen-rich solidus lines for PbS and  $\text{PbS}_{0.62}\text{Se}_{0.38}$  have been determined by means of Hall coefficient measurements on samples that were chalcogen-saturated by isothermal annealing and then quenched.

It has been demonstrated that the composition of  $\text{PbS}_{1-x}\text{Se}_x$  alloys can be conveniently and rapidly determined by using x-ray fluorescence to measure their Se content. A calibration curve was established by measurements on samples whose compositions had been determined by electron microprobe analysis.

## IV. PHYSICS OF SOLIDS

In the continuing rare-earth phosphor upconversion program, a study has been carried out of the  $\text{NaYF}_4:\text{Yb}, \text{Tm}$  anti-Stokes emission ( $\approx 0.81 \mu\text{m}$ ) which is of interest because it matches the absorption band of YAG:Nd. The onset of saturation effects in the phosphor appears to make the combination of a GaAs:Si diode with the phosphor less efficient than a GaAsP diode for pumping a YAG:Nd laser.

In one phase of the secondary electron emission program, the search for materials with high yields at low primary electron energies has turned to mixtures of insulating and conducting particles where the individual grains are small enough to allow tunneling to the conducting regions. Au-MgO films produced by sputtering look promising, and detailed studies of the effects on the yield of conducting and insulating substrates, substrate temperature, annealing and composition are now being carried out.

The free energy model, developed earlier for the insulator-metal transition in  $\text{Ti}_2\text{O}_3$ , has been extended to describe the high temperature transition in  $\text{V}_2\text{O}_3$ . A series of curves has been calculated which agrees qualitatively with the temperature dependence of the c-axis parameter observed in a series of Cr-doped  $\text{V}_2\text{O}_3$  samples.

Work on high resolution laser spectroscopy on NO continues. The Zeeman spectra of the  $\text{Q}(3/2)_{3/2}$  and  $\text{Q}(5/2)_{3/2}$  absorption lines, obtained by tuning these lines into coincidence with the  $\text{P}(15)_{9,8}$  emission line of a CO gas laser, exhibit fine structure, much larger than

that expected by present theory and the known molecular constants of NO. In other work, a current-tuned lead salt diode laser was used to study the R branch of NO at 77°K where nuclear hyperfine structure, obscured at room temperature because of Doppler broadening, is observed and found to be consistent with theory.

#### V. MICROELECTRONICS

At intervals, as has been done in the past, it seems appropriate to provide a general review of the overall Microelectronics Program. In addition to several major programs such as the Electron Beam Semiconductor development, LES IMPATT diode packaging, special mirror development, and sputtered metal oxide processing (some of which are described in Sec. V), there is preliminary development work in such areas as optoelectronic semiconductors, nuclear particle detector arrays and charge coupled devices.

The service base for routine work has increased slightly during this past quarter and about 50 work orders for thin film deposition, bonding and assembly, and other processing have been undertaken. Some of these requests involved routine processing of a number of pieces, while other requests required special processing of one or two parts.

The mask making for various laboratory programs continues at a relatively high level with 280 masks delivered during this quarter.

# REPORTS ON SOLID STATE RESEARCH

15 August through 15 November 1972

## PUBLISHED REPORTS

### Journal Articles\*

#### JA No.

3264	Magneto-Optical Properties	J. G. Mavroides	<u>Optical Properties of Solids</u> , F. Abeles, Ed. (North-Holland Publishing Co., Amsterdam, 1972), p. 355.
3857A	Comment on "Observation of Nonextremal Fermi Surface Orbita in Bulk Bismuth" – Author's Reply	V. E. Henrich	Phys. Rev. B <u>6</u> , 3151 (1972), DDC AD-752972
3967	Sealed Crucible Technique for Thermal Analysis of Volatile Compounds up to 2500°C: Melting Points of EuO, EuS, EuSe and EuTe	T. B. Reed R. E. Fahey A. J. Strauss	J. Crystal Growth <u>15</u> , 174 (1972), DDC AD-753368
3970	Observation of Nuclear Hyperfine Splitting in the Infrared Vibration-Rotation Absorption Spectrum of the NO Molecule	F. A. Blum K. W. Nill A. R. Calawa T. C. Harman	Chem. Phys. Letters <u>15</u> , 144 (1972), DDC AD-753369
4018	High Resolution Spectroscopy Using Magnetic-Field-Tuned Semiconductor Lasers	K. W. Nill F. A. Blum A. R. Calawa T. C. Harman	Appl. Phys. Letters <u>21</u> , 132 (1972), DDC AD-752970
4038	Tunable Infrared Laser Spectroscopy of Atmospheric Water Vapor	F. A. Blum K. W. Nill P. L. Kelley A. R. Calawa T. C. Harman	Science <u>177</u> , 694 (1972), DDC AD-752998
4045	NaYF <sub>4</sub> :Yb, Er – An Efficient Upconversion Phosphor	N. Menyuk K. Dwight J. W. Pierce	Appl. Phys. Letters <u>21</u> , 159 (1972), DDC AD-752985
4049	The Effect of Inhomogeneities in Acoustic-Surface-Wave Amplification	B. E. Burke Abraham Bers†	Appl. Phys. Letters <u>21</u> , 449 (1972), DDC AD-753309

\* Reprints available.

† Author not at Lincoln Laboratory.

JA No.

4053	Collisional Narrowing of Infrared Water-Vapor Transitions	R. S. Eng A. R. Calawa T. C. Harman P. L. Kelley A. Javan*	Appl. Phys. Letters <u>21</u> , 303 (1972), DDC AD-753003
4071	Double-Heterostructure GaAs:Si Diode Lasers	J. A. Rossi J. J. Hsieh	Appl. Phys. Letters <u>21</u> , 287 (1972), DDC AD-753005
4072	Submillimeter Spectroscopy	H. R. Fetterman H. R. Schlossberg* J. Waldman	Laser Focus <u>8</u> , 42 (1972), DDC AD-753006
4106	Identification of Donor Species in High-Purity GaAs Using Optically Pumped Submillimeter Lasers	H. R. Fetterman J. Waldman C. M. Wolfe G. E. Stillman C. D. Parker	Appl. Phys. Letters <u>21</u> , 434 (1972), DDC AD-753310

Meeting SpeechesMS No.

3090	Influence of Madelung Energy and Covalency on the Structure of $A^+B^{5+}O_3$ Compounds	J. A. Kafalas	Solid State Chemistry, Proceedings of 5th Materials Research Symposium, R. S. Roth and S. J. Schneider, Eds. (N. B. S. Special Publication 364, July 1972), p. 287
3120	Preparation and Structure of a Pyrochlore and Perovskite in the $BiRhO_{3+x}$ System	J. M. Longo P. M. Raccah J. A. Kafalas J. W. Pierce	Solid State Chemistry, Proceedings of 5th Materials Research Symposium, R. S. Roth and S. J. Schneider, Eds. (N. B. S. Special Publication 364, July 1972), p. 219

\* \* \* \* \*

## UNPUBLISHED REPORTS

Journal ArticlesJA No.

4036	Ferromagnetism	J. B. Goodenough	Accepted by Encyclopedia of Chemistry (Utet/Sansoni Edizioni Scientifiche, Firenze)
4043	Giant Quantum Oscillations in High Purity Bismuth: Search for Hole Fermi Surface Anomalies	V. E. Henrich	Accepted by Phys. Rev.

\* Author not at Lincoln Laboratory.

Reports

<u>JA No.</u>			
4068	Two-Phonon Deformation Potential	K. L. Ngai* E. J. Johnson	Accepted by Phys. Rev. Letters
4081	Electric Field Induced Transient Spin-Flip Raman Laser Pulses in InSb	A. Mooradian S. R. J. Brueck E. J. Johnson J. A. Rossi	Accepted by Appl. Phys. Letters
4083	Submillimeter Lasers Optically Pumped off Resonance	H. R. Fetterman H. R. Schlossberg* J. Waldman	Accepted by Optics Commun.
4087	PbS Photodiodes Fabricated by Sb <sup>+</sup> Ion Implantation	J. P. Donnelly T. C. Harman A. G. Foyt W. T. Lindley	Accepted by Solid State Electronics
4089	Exciton Levels in a Magnetic Field	N. Lee* D. M. Larsen B. Lax*	Accepted by J. Phys. Chem. Solids.
4094	Theory of the Spontaneous Spin-Flip Raman Lineshape in InSb	R. W. Davies	Accepted by Phys. Rev.
4097	High Resolution Photoconductivity Studies of Residual Shallow Donors in Ultrapure Ge	S. D. Seccombe D. M. Korn	Accepted by Solid State Commun.
4107	Procedure for Polishing PbS and PbS <sub>1-x</sub> Se <sub>x</sub>	G. A. Ferrante M. C. Lavine T. C. Harman J. P. Donnelly	Accepted by J. Electrochem. Soc.
4115	Anomalously High "Mobility" in GaAs	C. M. Wolfe G. E. Stillman D. L. Spears D. E. Hill* F. V. Williams*	Accepted by J. Appl. Phys.
4116	Growth of Crystals of V <sub>2</sub> O <sub>3</sub> and (V <sub>1-x</sub> Cr <sub>x</sub> ) <sub>2</sub> O <sub>3</sub> by the Tri-Arc Czochralski Method	J. C. C. Fan T. B. Reed	Accepted by Mater. Res. Bull.
MS-3338	Stripe-Geometry Pb <sub>1-x</sub> Sn <sub>x</sub> Te Diode Lasers	R. W. Ralston I. Melngailis A. R. Calawa W. T. Lindley	Accepted by IEEE J. Quantum Electron.
MS-3344	Photothermal Ionization of Shallow Donors in GaAs	G. E. Stillman C. M. Wolfe D. M. Korn	Accepted by Proc. 11th Intl. Conf. on the Physics of Semiconductors, Warsaw, Poland, 25-29 July 1972

\* Author not at Lincoln Laboratory.

JA No.

MS-3350	Small Bandgap Lasers and Their Uses in Spectroscopy	A. R. Calawa	Accepted by Proc. C.S.A.T.A. Symp. on "The Physics and Technology of Semiconductor Light Emitters and Detectors," Pugnochiuso, Italy, 4-10 September 1972
MS-3351	Small Bandgap Semiconductor Infrared Detectors	I. Melngailis	
MS-3353	Dependence of Growth Temperature on Carrier Gas Velocity in Open Tube Transport	T. B. Reed W. J. LaFleur	Accepted by J. Crystal Growth
MS-3367	Pseudobinary Phase Diagram and Existence Regions for $\text{PbS}_{1-x}\text{Se}_x$	A. J. Strauss T. C. Harman	Accepted by J. Electronic Materials
MS-3369A	Proton Guarded GaAs IMPATT Diodes	R. A. Murphy W. T. Lindley D. F. Peterson A. G. Foyt C. M. Wolfe C. E. Hurwitz J. P. Donnelly	Accepted by Proc. 4th Int'l. Symp. on GaAs and Related Compounds, Boulder, Colorado, 25-27 September 1972
MS-3373	The Structure of $\text{La}_2\text{CuO}_4$ and $\text{LaSrVO}_4$	J. M. Longo P. M. Raccah	Accepted by J. Solid State Chem.
MS-3391	Narrow-Gap Semiconductor Lasers and Detectors	I. Melngailis	Accepted by Proc. 1972 Conf. on Solid State Devices, Tokyo, Japan, 30-31 August 1972
MS-3392	Schottky Barrier GaAs Electron Beam Semiconductor Amplifier (EBIRD)	W. T. Lindley W. E. Krag C. M. Wolfe R. J. Sasiela R. A. Murphy C. E. Hurwitz D. F. Kostishack A. J. Yakutis A. G. Foyt	Accepted by Proc. 4th Int'l. Symp. on GaAs and Related Compounds, Boulder, Colorado, 25-27 September 1972

Meeting Speeches\*

MS No.

3090A	High Pressure Synthesis	J. A. Kafalas	Dept. of Chemistry Seminar, Yeshiva University New York, New York 18 October 1972
3248	High Resolution Spectroscopy in the $5 \mu\text{m}$ Region Using Tunable Semiconductor Lasers	F. A. Blum K. W. Nill	Gordon Research Conference on Infrared Spectroscopy, Meriden, New Hampshire, 14-18 August 1972

\* Titles of Meeting Speeches are listed for information only. No copies are available for distribution.

Reports

MS No.

3318C	High Resolution Infrared Spectroscopy Using Tunable Semiconductor Lasers	K. W. Nill F. A. Blum	4th Northeast Regional Meeting, American Chemical Society, Hartford, Connecticut, 18 October 1972
3337A	Tunable Semiconductor Lasers	A. Mooradian	Gordon Research Conference on Infrared and Raman Spectroscopy, Meriden, New Hampshire, 14-18 August 1972
3337B	Tunable Semiconductor Lasers	A. Mooradian	Seminar, Lawrence Livermore Laboratory, University of California, Livermore, California, 21 August 1972
3337C	Tunable Semiconductor Lasers	A. Mooradian	IEEE Seminar, Tufts University, Medford, Massachusetts, 17 October 1972
3337D	Tunable Semiconductor Lasers and Their Applications	A. Mooradian	Seminar on Laser Technology, George Washington University, Washington, D.C., 19 October 1972
3345	An Integrated Intermediate Frequency Amplifier-Limiter	James K. Roberge* William H. McGonagle	1972 Government Microcircuit Applications Conference, San Diego, California, 10-12 October 1972
3350	Small Bandgap Lasers and Their Uses in Spectroscopy	A. R. Calawa	C.S.A.T.A. Symposium on "The Physics and Technology of Semiconductor Light Emitters and Detectors," Pugnochiuso, Italy, 4-10 September 1972
3351	Small Bandgap Semiconductor Infrared Detectors	I. Melngailis	C. S. A. T. A. Symposium on "The Physics and Technology of Semiconductor Light Emitters and Detectors," Pugnochiuso, Italy, 4-10 September 1972
3367	Pseudobinary Phase Diagram and Existence Regions for PbS <sub>1-x</sub> Se <sub>x</sub>	A. J. Strauss T. C. Harman	Electronic Materials Conference, Boston, Massachusetts 28-30 August 1972
3369A	Proton Guarded GaAs IMPATT Diodes	R. A. Murphy W. T. Lindley D. F. Peterson A. G. Foyt C. M. Wolfe C. E. Hurwitz J. P. Donnelly	4th Intl. Symp. on GaAs and Related Compounds, Boulder, Colorado, 25-27 September 1972

\* Author not at Lincoln Laboratory.

MS No.

3373	The Structure of $\text{La}_2\text{CuO}_4$ and $\text{LaSrVO}_4$	J. M. Longo P. M. Raccah	Northeastern Regional Meeting, American Chemical Society, New York, New York 27 August-1 September 1972
3374	Preparation of Infrared-to-Visible Upconversion Phosphors Based on Hexagonal $\text{NaYF}_4$	J. W. Pierce E. J. Delaney K. Dwight N. Menyuk	
3391	Narrow-Gap Semiconductor Lasers and Detectors	I. Melngailis	1972 Conf. on Solid State Devices, Tokyo, Japan, 30-31 August 1972
3392	Schottky Barrier GaAs Electron Beam Semiconductor Amplifier (EBIRD)	W. T. Lindley W. E. Krag C. M. Wolfe R. J. Sasiela R. A. Murphy C. E. Hurwitz D. F. Kostishack A. J. Yakutis A. G. Foyt	4th Intl. Symp. on GaAs and Related Compounds, Boulder, Colorado, 25-27 September 1972
3407	Use of Tunable Semiconductor Lasers in High Resolution Infrared Spectroscopy Near $5 \mu\text{m}$	K. W. Nill F. A. Blum	"Tunable Lasers" Conference, Heriot-Watt University, Edinburgh, Scotland, 6-8 September 1972
3412	High Frequency Surface Wave Transducers Fabricated by X-Ray Lithography	D. L. Spears H. I. Smith	IEEE Ultrasonics Symp., Boston, Massachusetts, 4-6 October 1972
3415	High Resolution Molecular Spectroscopy Near $5 \mu\text{m}$ Using Tunable Semiconductor Lasers	F. A. Blum K. W. Nill A. R. Calawa T. C. Harman	1st International Conference on Spectral Lines, Knoxville, Tennessee, 28 August-1 September 1972
3455	Ion Implantation and Some Applications to Compound Semiconductor Devices	J. P. Donnelly	Colloquium, Division of Electrical Engineering and Applied Physics, Case Western Reserve University, Cleveland, Ohio, 2 November 1972
3459	High Resolution Photoconductivity Studies of Residual Shallow Donors in Ultrapure Germanium as Studied by Fourier Transform Spectroscopy	D. M. Korn	Physics Seminar, 3M Central Research Laboratory, St. Paul, Minnesota, 10 November 1972

# ORGANIZATION

## SOLID STATE DIVISION

A. L. McWhorter, *Head*  
P. E. Tannenwald, *Associate Head*  
C. R. Grant, *Assistant*

### QUANTUM ELECTRONICS

A. Mooradian, *Leader*  
P. L. Kelley, *Associate Leader*

Brueck, S. R. J.      Johnson, E. J.  
Chinn, S. R.      Moulton, P. F.\*  
Eng, R. S.      Pine, A. S.  
Hancock, R. C.      Rossi, J. A.  
Heckscher, H.

### ELECTRONIC MATERIALS

J. B. Goodenough, *Leader*  
A. J. Strauss, *Associate Leader*

Anderson, C. H., Jr.      Lavine, M. C.†  
Batson, D. A.      Mastromattei, E. L.  
Button, M. J.      Mikkelsen, J. C.  
Delaney, E. J.      Mroczkowski, I. H.  
Fnhey, R. E.      Owens, E. B.  
Fan, J. C. C.      Pantano, J. V.  
Finn, M. C.      Pierce, J. W.  
Hong, H. Y-P.      Plonko, M. C.  
Hsieh, J. J.      Reed, T. B.  
Iseler, G. W.      Tracy, D. M.  
Kafalas, J. A.      Zavracky, P. M.  
LaFleur, W. J.

### MICROELECTRONICS

R. E. McMahon, *Leader*

Bachner, F. J.      Gray, R. V.  
Beatrice, P. A.      McGonagle, W. H.  
Burke, B. E.      Mountain, R. W.  
Clough, T. F.      Pichler, H. H.  
Gohen, R. A.      Smythe, D. I.  
Durant, G. L.      Wilde, R. E.  
Grant, L. L.

### SOLID STATE PHYSICS

J. G. Mavroides, *Co-Leader*  
H. J. Zeiger, *Co-Leader*

Allen, J. W.      Groves, S. H.  
Animulu, A. O. E.      Henrich, V. E.  
Barch, W. E.      Johnson, L.\*  
Blum, F. A., Jr.      Kolesar, D. F.  
Davies, R. W.      Korn, D. M.  
DeFeo, W. E.      Larsen, D. M.  
Dresselhaus, G. F.      Menyuk, N.  
Dwight, K., Jr.      Nill, K. W.  
Feldman, B.      Purker, C. D.  
Fetterman, H.

### APPLIED PHYSICS

I. Melngailis, *Leader*  
A. G. Foyt, *Assistant Leader*  
T. C. Harman, *Assistant Leader*

Belanger, L. J.      Lindley, W. T.  
Calawa, A. R.      McBride, W. F.  
Carter, F. B.      Murphy, R. A.  
DeMeo, N.      Orphanos, W. G.  
Donnelly, J. P.      Paladino, A. E.  
Ferrante, G. A.      Ralston, R. W.  
Hirshowitz, C. E.      Spears, D. L.  
Krohn, L., Jr.      Stillman, G. E.  
Leonberger, F. F.\*      Walpole, J. N.  
Lincoln, G. A., Jr.      Wolfe, C. M.

### MICROSOUND

E. Stern, *Leader*

Alusow, J. A.      Li, R. C. M.  
Brogan, W. T.      Melngailis, J.  
Efremow, N.      Smith, H. I.  
Kalish, D.      Smith, J. M.  
Kerman, W. C.      Williamson, R. C.

\* Research Assistant

† Part Time

## I. SOLID STATE DEVICE RESEARCH

### A. FIELD-PLATE-GUARDED InSb PHOTODIODE ARRAYS

Linear arrays of 20 closely spaced InSb n-p junction photodiodes have been fabricated using the techniques of proton bombardment and field-plate-guarding. High quality single-element detectors made by use of these techniques have been described in previous reports.<sup>1,2</sup> The arrays exhibit similarly good elemental detector performance as well as excellent uniformity among elements of an array. In addition, the yield of good arrays per wafer has been unusually high.

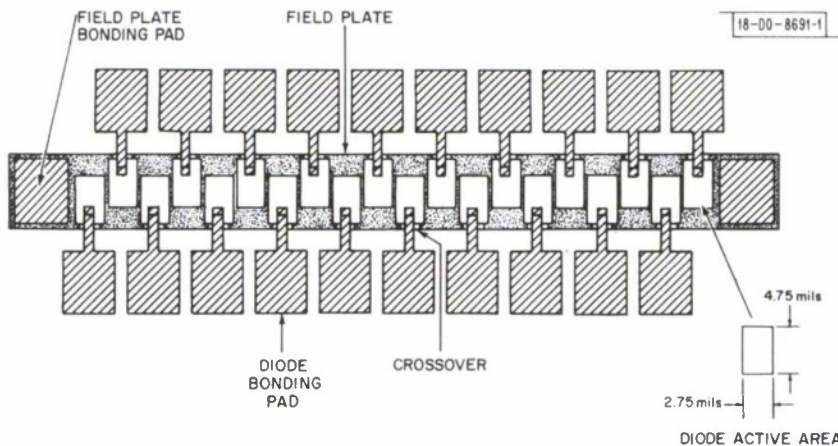


Fig. I-1. Artist's sketch of 20 element InSb photodiode array. Spacing between adjacent diodes is approximately 5  $\mu\text{m}$ .

An artist's sketch of the array is shown in Fig. I-1. The fabrication proceeds in the following manner. A wafer of p-type InSb, with carrier concentration approximately  $2 \times 10^{15} \text{ cm}^{-3}$  at 77°K, is chemically etched or electropolished to remove approximately 10  $\mu\text{m}$  of material. The freshly etched surface is immediately coated with 1000  $\text{\AA}$  of silicon oxynitride, formed by the pyrolytic reaction of  $\text{SiH}_4$ ,  $\text{O}_2$  and  $\text{NH}_3$  in a  $\text{N}_2$ -rich atmosphere at 180°C. This silicon oxynitride, being somewhat permeable, is overcoated with a sealing layer of 1500  $\text{\AA}$  of sputtered  $\text{SiO}_2$  and thence by sequential sputtering with 300  $\text{\AA}$  of Cr, 8000  $\text{\AA}$  of Au and 250  $\text{\AA}$  of Ti. As in the previously described single-element detectors,<sup>1,2</sup> the thick Au will become the bombardment mask as well as the field plate. The underlayer of Cr is for adhesion of the Au to the  $\text{SiO}_2$  and the Ti is to promote adhesion of a subsequent layer of  $\text{SiO}_2$  to the Au. The Cr-Au-Ti sandwich is patterned and etched to form the field plate structure as shown by the stippled area in the sketch. The "windows" in the field plate, which will become the diodes, are 4.75  $\times$  2.75 mils, and the spacing between them is 5  $\mu\text{m}$ . One-mil-square holes are opened in the  $\text{SiO}_2$ -SiON layer and plated with 700  $\text{\AA}$  of Au. These areas will form the diode contacts.

The wafer is then bombarded with a beam of 100-keV protons, for a total dose of  $1.4 \times 10^{14} \text{ cm}^{-2}$ . The area exposed to the beam is converted to n-type, while that shielded from the beam by the gold field plate remains p-type. As discussed previously,<sup>1</sup> the tapered edge of the

## Section I

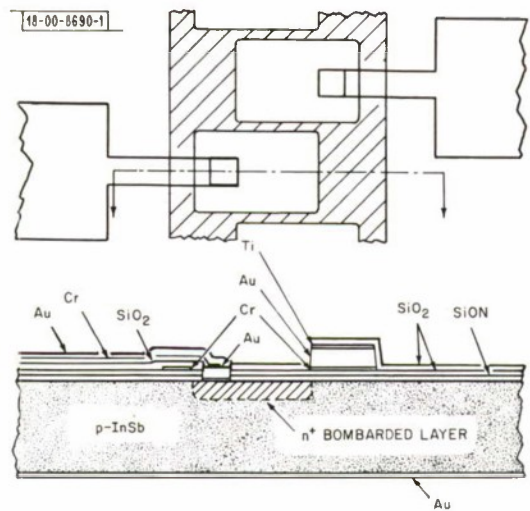


Fig. I-2. Sketch of two adjacent elements of InSb array with a cross-sectional view through one of the diodes.

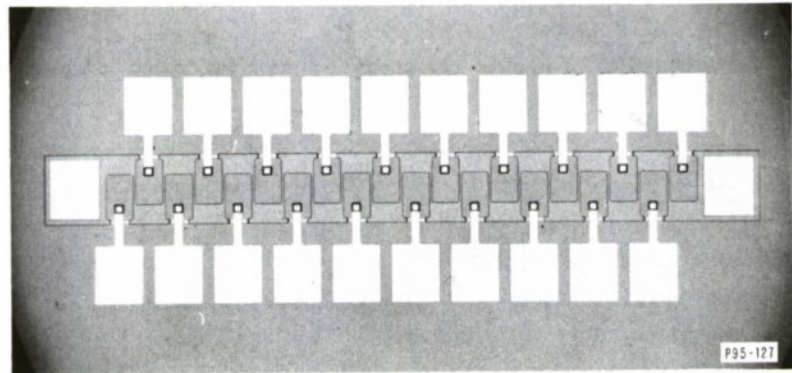


Fig. I-3. Photograph of a completed array before bonding of leads.

gold, produced by the etching, causes the junction edge to be slightly under the edge of the field plate in perfect alignment.

In order to provide bonding pads away from the active diode area, a connection between the diode contact and pad, crossing over the field plate, must be provided. This is accomplished by removing the Ti and Au of the field plate at the crossover point, as indicated in the sketch. The thin Cr layer, which is easily insulated and crossed, remains and provides field plate continuity around the entire perimeter of each diode. A 3000- $\text{\AA}$  layer of  $\text{SiO}_2$  is sputtered over the entire wafer to insulate the crossover. After reopening of the contact holes, a 300  $\text{\AA}$  layer of Cr and 1  $\mu\text{m}$  of Au is sputtered on and patterned to form the bonding pads and connecting bridges to the diodes.

Finally, areas for bonding of leads are exposed at the ends of the field plate by removal of the  $\text{SiO}_2$  and Ti. The back of the wafer is then sandblasted and Au plated to form the contact to the p-type substrate. A sketch of two adjacent diodes and a cross section through one of them is shown in Fig. 1-2. A photograph of a completed 20-element array is shown in Fig. 1-3.

The wafer is scribed and cleaved into individual or groups of arrays which are mounted with indium on a sapphire header. Gold wires are bonded on the array pads and stitched to pads on the header. The entire assembly is then mounted in a liquid nitrogen dewar for testing.

Characteristic	Measured at	
	Lincoln Laboratory	Night Vision Laboratory
$D^*_\lambda$ (5 $\mu\text{m}$ ) ( $\text{cmHz}^{1/2}/\text{W}$ )	$(6.0 \pm 0.2) \times 10^{10}$	$(7.4 \pm 0.6) \times 10^{10}$
$\eta$ (percent)	$20 \pm 3$	$17 \pm 1$
$I_{rev}$ (0.1 V) (nA)	$55 \pm 2$	$42 \pm 3$
Cross talk (percent)	—	<1

Arrays were tested both at this Laboratory and by R. Longshore at the U.S. Army Night Vision Laboratory. Results of these measurements for a typical array are tabulated in Table I-1. A field plate voltage of zero volts was found to be optimum for this array. The spread in values listed in the table are among the individual elements of the array. The uniformity in the various quantities should be noted. The somewhat lower values of  $D^*$  obtained in our measurements is attributed to the poorer noise performance of the amplifier used by us. (Even though the noise is largely due to the background photon flux, a smaller fraction is still due to the amplifier.)

The quantum efficiencies of the diodes in this array, and in fact of all arrays on this particular wafer, were abnormally low. For reasons not presently understood, an occasional wafer will exhibit somewhat reduced quantum efficiencies. A more typical value is 30 to 35 percent, which would result in  $D^*$  values approximately 50 percent higher.

## Section I

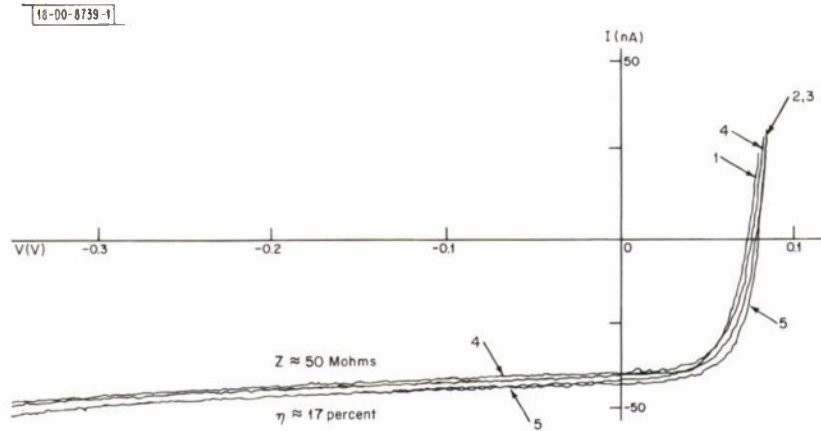


Fig. I-4. I-V characteristics of five diodes in the array tested by the Night Vision Laboratory. The characteristics of the remaining elements of the array fall on top of those shown here and are omitted for clarity.

The difference in reverse current of the diodes as measured at the two laboratories is due simply to differences in ambient background. (The reverse current is primarily photocurrent due to the background radiation.) Reverse I-V characteristics for five of the diodes are shown in Fig. I-4. The largest spread is between elements 4 and 5. The characteristics of the rest of the diodes fall on top of the ones shown and are omitted for clarity.

The cross talk between adjacent diodes was measured at the Night Vision Laboratory by focusing a small chopped spot of radiation on one diode and measuring the signal at adjacent diodes. At 1000 Hz, the only frequency at which the measurements were made, the cross-talk signal was below the level of the system noise and hence we conclude that the cross talk was less than 1 percent. Further measurements at higher frequencies are in progress.

Of the 50 arrays on the wafer from which the above device was taken, 25 arrays were completely good and usable. Eighteen of the remaining 25 had defects due to photolithographic errors and/or dirt. These problems are easily solved with improved techniques. Only seven of the 50 arrays had bad diodes. This extremely high yield will prove to be even more important for the much larger arrays presently being fabricated in conjunction with the one-dimensional InSb array vidicon program.

C. E. Hurwitz  
A. G. Foyt  
W. T. Lindley

### B. PbS PHOTODIODES FABRICATED BY Sb<sup>+</sup> ION IMPLANTATION

Using Sb<sup>+</sup> ion implantation to create the n-type layer, n-p junction photodiodes in PbS have been fabricated. The Sb<sup>+</sup> implantation process is similar to that previously used in the fabrication of PbTe photodiodes.<sup>1,3</sup> The zero-bias resistance of 15-mil-square PbS diodes was typically 200 ohms at 300°K,  $5 \times 10^4$  ohms at 195°K and  $5 \times 10^9$  ohms at 77°K. Peak detectivities occurred at 2.55, 2.95 and 3.4 μm at 300°, 195° and 77°K, respectively. The corresponding measured detectivities were  $4.8 \times 10^9$ ,  $1.1 \times 10^{11}$  and  $4.2 \times 10^{12} \text{ cmHz}^{1/2}/\text{W}$ . The 77°K detectivity was measured in a reduced background and was amplifier noise limited. Peak quantum efficiencies were typically 50 to 60 percent.

The PbS crystals used in these experiments were grown by the Bridgman method. In order to obtain p-type material, as-grown samples 0.44 cm in thickness were isothermally annealed in a sulfur-rich PbS atmosphere for one week at 700°C and an additional week at 500°C. At 300°K, these annealed crystals had a p-type carrier concentration of  $3 \times 10^{18} \text{ cm}^{-3}$  and a mobility of  $500 \text{ cm}^2/\text{V}\cdot\text{sec}$ . At 77°K, the p-type carrier concentration was unchanged and the mobility increased to  $9000 \text{ cm}^2/\text{V}\cdot\text{sec}$ .

Prior to implantation, the annealed samples were further cut into slices  $0.44 \times 1 \times 0.1 \text{ cm}$ . These slices were then polished and free-etched in a highly agitated aqua regia solution at 40°C until all visually observable surface damage was removed. The entire etching procedure has been described in a previous report.<sup>4</sup> Using a silane-oxygen reaction,  $1000 \text{ \AA}$  of pyrolytic  $\text{SiO}_2$  was then deposited on the front face of each sample. This oxide is put down for alignment purposes so that the implanted areas can be distinguished after post-implantation processing. The PbS samples were then coated with a thick layer of photoresist and an array of 15-mil squares on 20-mil centers opened in this photoresist and the alignment oxide. This photoresist is sufficiently thick ( $\sim 5 \mu\text{m}$ ) to completely stop the  $\text{Sb}^+$  ions used in the subsequent ion implantation step and therefore acts as a suitable ion implantation mask. The  $\text{Sb}^+$  ion implantation was carried out with the PbS samples at room temperature using 400-keV  $\text{Sb}^+$  ions. A total ion fluence of  $2.5 \times 10^{14} \text{ cm}^{-2}$  was used in these experiments. For control purposes, several squares were usually shielded from the  $\text{Sb}^+$  ion beam.

Following implantation, the photoresist implantation mask was removed and each sample was coated with a  $1500\text{-\AA}$  layer of pyrolytic  $\text{SiO}_2$  at 400°C. The samples were held at 400°C for a total anneal time of 5 minutes (including the time at temperature spent depositing the  $\text{SiO}_2$ ). It appears that this anneal step is sufficient to effectively anneal out the radiation damage caused by the room temperature  $\text{Sb}^+$  ion implantation. Holes were then opened in the oxide and gold contacts were electroplated on the sample. A completed diode with one contact on the n-type  $\text{Sb}^+$  implanted layer is illustrated in Fig. 1-5. In initial experiments, four contacts instead of one were plated on each diode so that electrical evaluation of the implanted region could be carried out.

Hall effect measurements of the van der Pauw<sup>5</sup> type and current-voltage measurements between various contacts on these initial samples at both 300° and 77°K (these measurements are discussed more fully in a previous publication)<sup>6</sup> indicated that the  $\text{Sb}^+$  implanted areas were converted to n-type while unimplanted portions of the crystal remained p-type. Thermoelectric probe measurements at 77°K substantiated these results. At 77°K, the van der Pauw<sup>5</sup> measurement gave an n-type sheet carrier concentration in the  $\text{Sb}^+$  implanted region of  $5 \times 10^{14} \text{ cm}^{-2}$ , which is twice the total  $\text{Sb}^+$  dose. At 300°K, the measured sheet carrier concentration was slightly higher due to leakage through the substrate. It is not clear at the present time whether the high

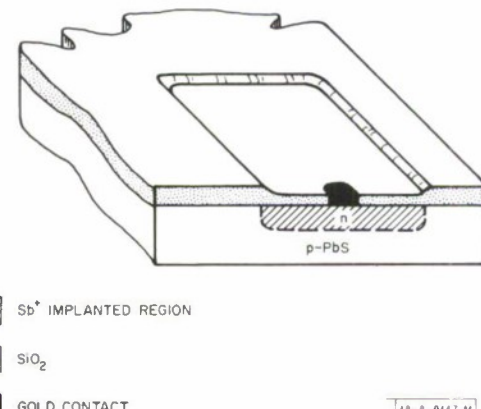


Fig. 1-5. Photodiode sample structure fabricated using  $\text{Sb}^+$  ion implantation to create the n-type layer.

## Section I

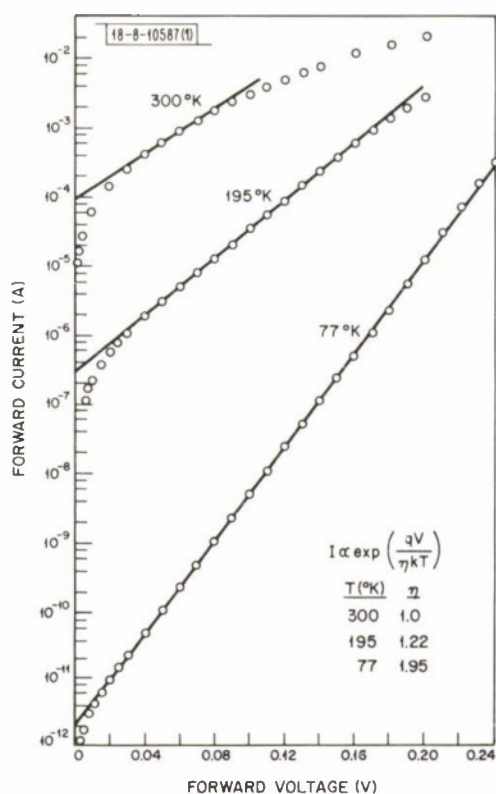


Fig. I-6. Forward current-voltage characteristic in a reduced background of a 15-mil-square Sb<sup>+</sup> implanted PbS diode at 300°, 195° and 77°K.

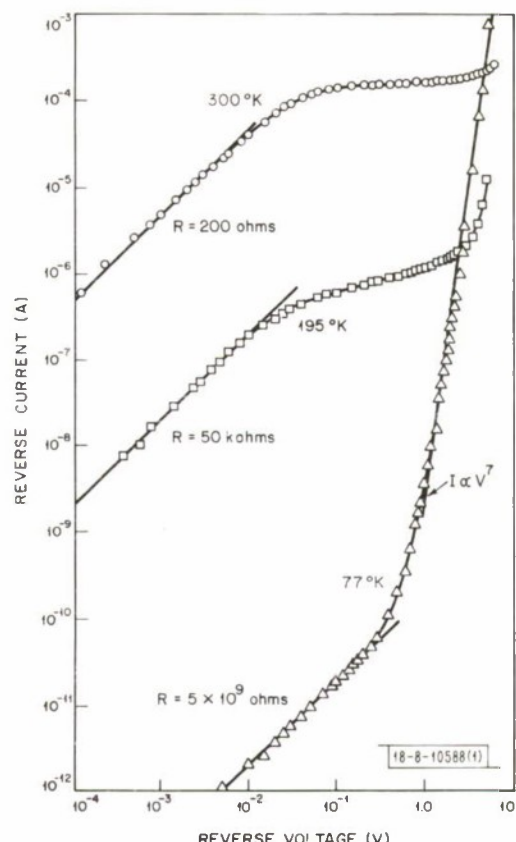


Fig. I-7. Reverse current-voltage characteristic in a reduced background of a 15-mil-square Sb<sup>+</sup> implanted PbS diode at 300°, 195° and 77°K.

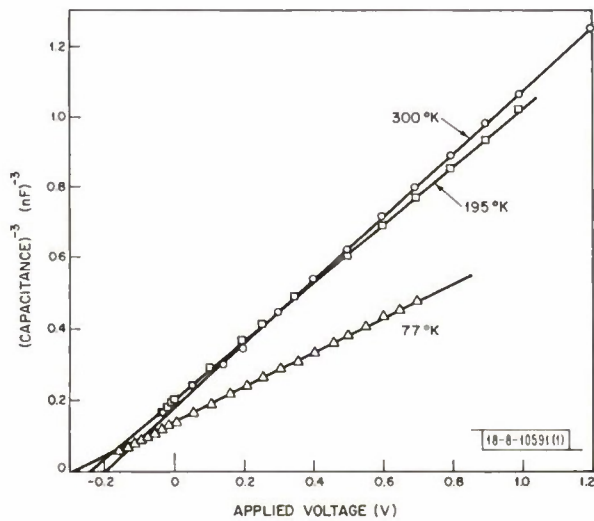


Fig. I-8. The  $(\text{capacitance})^{-3}$  as a function of applied voltage of a 15-mil-square Sb<sup>+</sup> implanted PbS diode at 300°, 195° and 77°K.

measured sheet carrier concentration is an artifact of the measurement or has some physical significance.

N-p junction current-voltage characteristics with normal photodiode response were observed between the n-type implanted region and the p-type substrate. 15-mil-square photodiodes prepared by the Sb<sup>+</sup> ion implantation technique have exhibited zero-bias resistances of 200 ohms for a resistance-area product of 0.28 ohm-cm<sup>2</sup> at 300°K; 50 kohms for a resistance-area product of 70 ohm-cm<sup>2</sup> at 195°K; and 5 × 10<sup>9</sup> ohms for a resistance-area product of 7 × 10<sup>6</sup> ohm-cm<sup>2</sup> at 77°K. The forward and reverse current-voltage characteristics of a typical diode in reduced background at 300°, 195° and 77°K are shown in Figs. I-6 and I-7, respectively. At all three temperatures, for qV ≥ several kT (where V is the applied voltage), the forward current is given by  $I = I_0 \exp(qV/\eta kT)$ . At 300°K, although there is some voltage drop in the forward direction due to series resistance, it appears that  $\eta \approx 1$ . The reverse current at this temperature shows a marked current saturation at about 150 μA. These 300°K current-voltage characteristics are in agreement with a diffusion current diode model. At 195°K,  $\eta \approx 1.22$ , indicating that there may be some recombination-generation current adding to the total current. The reverse current again shows some saturation, although the slope of the log I vs log V plot is greater than at 300°K. At 77°K,  $\eta \approx 1.95$ , indicating that recombination-generation currents are probably the dominant transport mechanism. In the reverse direction, the linear low voltage portion of the characteristic is followed by a soft power law breakdown without any saturation of the reverse current. Although the nature of this breakdown is not completely understood at the present time, it should be noted that power law breakdowns of this type have previously been explained by tunneling.<sup>7</sup>

The capacitance-voltage characteristics of these diodes exhibit a  $1/C^3 \propto V$  dependence, indicating that the effective carrier concentration is linearly graded. However, as shown in Fig. I-8, the slope of  $1/C^3$  vs V decreases with decreasing temperature. The slope decreases only slightly from 0.89 to 0.81/nF<sup>3</sup>-V between 300° and 195°K. Between 195° and 77°K, however, the slope decreases substantially to 0.48/nF<sup>3</sup>-V at 77°K. This observed temperature dependence is opposite to that normally expected if de-ionization of impurities or defects occurred in the junction as the temperature was lowered. It might possibly be explained by a paraelectric behavior as discussed by R. T. Bate, *et al.*<sup>8,9</sup> for PbTe and pseudobinaries based on PbTe. However, the data points cannot be fit by assuming a dielectric constant which obeys a simple Curie law dependence,  $\epsilon_s^{-1} \propto (T - T_c)$ , where  $\epsilon_s$  is the dielectric constant, T the temperature in °K and  $T_c$  the Curie temperature.<sup>8,9</sup> From our data, it appears that the dielectric constant saturates with increasing temperature.

The zero-bias capacitance of these diodes was typically 1730 pF at 300°K, 1700 pF at 195°K and 1910 pF at 77°K. The zero-bias RC time constants calculated at the three temperatures are therefore  $3.4 \times 10^{-7}$ ,  $8.5 \times 10^{-5}$  and 9.5 sec, respectively. The extrapolation of  $1/C^3$  to zero gives diffusion voltages of  $V_D = 0.20$  V at 300°K, 0.24 V at 195°K and 0.29 V at 77°K.

Blackbody responsivity, relative spectral response and noise measurements were carried out with the PbS photodiode at 300°, 195° and 77°K. The blackbody responsivity was measured using both a 500° and an 800°K blackbody at chopping frequencies between 20 and 1000 Hz. Relative spectral response was measured using a prism spectrometer, and the system noise was measured using a low noise, high impedance preamplifier and a wave analyzer. During the

## Section I

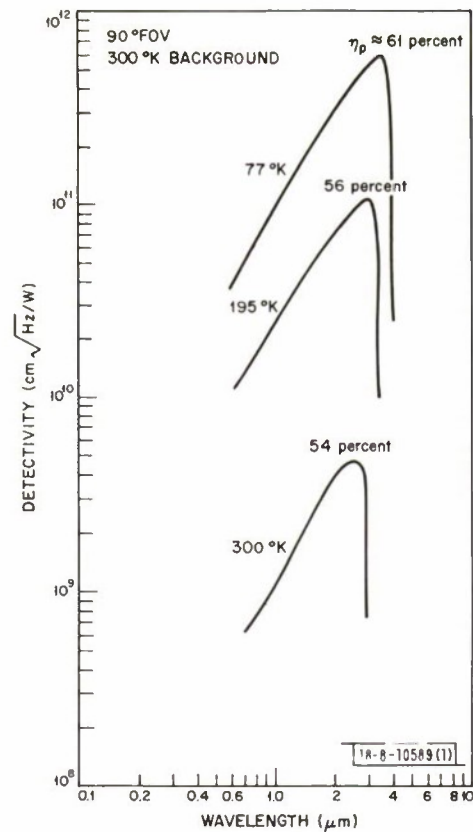


Fig. I-9. Detectivity of a 15-mil-square  $\text{Sb}^+$  implanted  $\text{PbS}$  diode as a function of wavelength at 300°, 195° and 77°K.

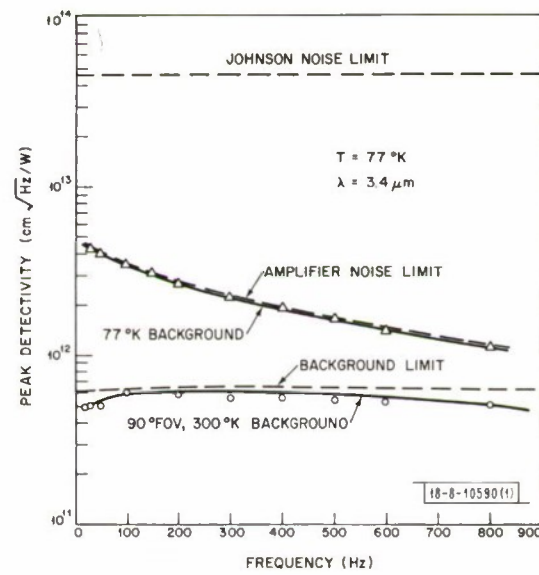


Fig. I-10. Peak detectivity at  $3.4 \mu\text{m}$  of a 15-mil-square  $\text{PbS}$  diode at 77°K as a function of background and frequency.

measurements, the diode voltage was held within  $\pm 1$  mV of the desired value using a high resistance metal film resistor and a variable power supply. The resistance of the metal film resistor was kept high enough at all times so that it did not load the photodiode-amplifier system or add any significant contribution to the system noise. The zero-bias detectivity as a function of wavelength in a 90° FOV, 300°K background of a typical diode at 100 Hz is shown in Fig. I-9.

At 300° and 195°K, the detectivity is Johnson noise limited due to the zero-bias resistance of the diode. At 300°K, the peak detectivity, which occurs at 2.55  $\mu\text{m}$ , is  $4.8 \times 10^9 \text{ cmHz}^{1/2}/\text{W}$  with a peak quantum efficiency of 54 percent. This value is the external quantum efficiency, uncorrected for reflection and without an antireflection coating. At 195°K, the peak detectivity shifts to 2.95  $\mu\text{m}$  and increases to  $1.1 \times 10^{11} \text{ cmHz}^{1/2}/\text{W}$ . The peak quantum efficiency at 195°K is 56 percent.

At 77°K, the detectivity in the 90° FOV, 300°K background is essentially background limited. The peak detectivity which occurs at 3.4  $\mu\text{m}$  is  $6 \times 10^{11} \text{ cmHz}^{1/2}/\text{W}$  with a peak quantum efficiency of 61 percent. The peak detectivity, which increased due to a decrease in noise as the background was reduced, is plotted as a function of frequency and background in Fig. I-10. The points plotted on this figure were obtained in the following manner. The 800°K blackbody responsivity was measured as a function of frequency with a 90° FOV, 300°K background and an f/6 (9.5°) FOV, 300°K background, and was found to be essentially independent of aperture and to decrease with increasing frequency according to the RC time constant. The blackbody responsivity was therefore assumed to be independent of background. The relative spectral response was also assumed to be independent of background. The peak detectivity obtained from these measurements and measurements of the total system noise as a function of frequency and background are those plotted in Fig. I-10. For simplicity, only the 90° FOV, 300°K background and 77°K background (diode completely shielded) points are plotted in Fig. I-9. The f/6 FOV, 300°K background points were identical to the 77°K background points at the higher frequencies and only about 20 percent lower at the lowest frequency used in these measurements.

With a 90° FOV, 300°K background, the 77°K detectivity is essentially background limited and relatively independent of frequency from 20 to 800 Hz. There is a slight rolloff, however, in detectivity at both low and high frequencies. The rolloff below 100 Hz indicates that the diode is exhibiting some 1/f noise. At higher frequencies, the amplifier noise becomes important due to the RC ( $RC = 5 \times 10^9 \text{ ohms} \times 1900 \text{ pF} = 9.5 \text{ sec}$ ) rolloff in both the responsivity and diode noise. With the 77°K background (the diode completely shielded) the detectivity is amplifier noise limited over the entire range of measurements. The measured detectivity increased from  $1.1 \times 10^{12} \text{ cmHz}^{1/2}/\text{W}$  at 800 Hz to  $4.2 \times 10^{12} \text{ cmHz}^{1/2}/\text{W}$  at 30 Hz. The theoretical Johnson noise limit of this diode is  $4.6 \times 10^{13} \text{ cmHz}^{1/2}/\text{W}$ , an order of magnitude higher than the measured value at 30 Hz.

The peak detectivity as a function of reverse voltage of a typical diode at 300°, 195° and 77°K has been measured and is plotted in Fig. I-11. The shape of the relative spectral response did not change with increasing reverse voltage over the range of measurements. At 300°K [Fig. I-11(a)] and 195°K [Fig. I-11(b)] the detectivity decreases with increasing voltage over the frequency range of measurements. The detectivity at both temperatures shows marked saturation corresponding to the saturation noted in the reverse current. The measured noise of this diode with an applied reverse voltage at both 300° and 195°K is substantially higher than the

## Section I

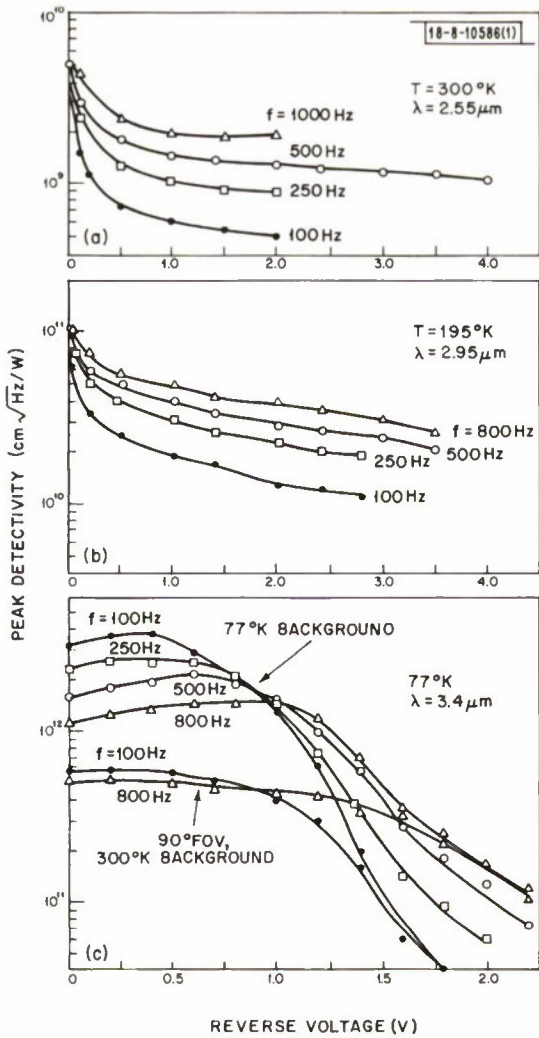


Fig. I-11. Peak detectivity of a 15-mil-square PbS diode as a function of reverse voltage and frequency at (a)  $300^\circ\text{K}$ , (b)  $195^\circ\text{K}$  and (c)  $77^\circ\text{K}$ .

calculated shot noise due to the reverse current. From reverse current shot noise considerations only, one would expect the reverse bias detectivity before breakdown to be slightly higher than the zero-bias detectivity. It should also be noted that in reverse bias the detectivity increases with increasing frequency. These data indicate that the diode is exhibiting excess  $1/f$  noise. On a diode with a poor ohmic contact, it was found that the excess noise was substantially higher than on a typical diode. It is therefore possible that at least part of the excess  $1/f$  noise is due to contacts.

At  $77^\circ\text{K}$ , in a  $90^\circ$  FOV,  $300^\circ\text{K}$  background, the detectivity remains fairly constant with increasing voltage until the diode begins to draw appreciable reverse current. At this point the diode begins to exhibit some excess  $1/f$  noise. With a  $77^\circ\text{K}$  background, the detectivity is essentially amplifier noise limited until breakdown voltage is reached. The measured detectivity actually increases with reverse bias in this region, since the responsivity, which is RC limited, increases due to the decrease in capacitance with reverse bias. Also, the detectivity in this region is higher at low frequencies. As the diode begins to draw appreciable current, the detectivity

becomes diode current noise limited and decreases rapidly, again exhibiting a  $1/f$  excess noise characteristic.

Photodiodes in  $\text{PbS}_{1-x}\text{Se}_x$  have also been fabricated using this  $\text{Sb}^+$  implantation technique and will be discussed in a future report.

J. P. Donnelly A. G. Foyt  
T. C. Harman W. T. Lindley

### C. PHOTODIODES FABRICATED IN EPITAXIAL PbTe BY $\text{Sb}^+$ ION IMPLANTATION

We have previously reported the use of  $\text{Sb}^+$  ion implantation to fabricate p-n junction PbTe diodes in bulk PbTe crystals.<sup>1,3</sup> Recently we have extended this technique to thin films of epitaxial PbTe grown on  $\text{BaF}_2$  (Ref. 10 and 11). The epitaxial thin film PbTe used in these experiments was supplied by H. Holloway of Ford Motor Company. At 77°K, these films had p-type carrier concentrations of  $\sim 5 \times 10^{16} \text{ cm}^{-3}$  and carrier mobilities of  $\sim 15,000 \text{ cm}^2/\text{V}\cdot\text{sec}$ . The  $\text{Sb}^+$  implantations were made into the as-grown PbTe surfaces. Otherwise, the  $\text{Sb}^+$  implantation procedure was the same as that previously used in bulk PbTe.<sup>3</sup>

At 77°K, 15-mil-square photodiodes had typical zero-bias resistances of 1 megohm corresponding to a resistance area product of  $1.4 \times 10^3 \text{ ohms}\cdot\text{cm}^2$ . The zero-bias capacitance of these diodes was typically about 1000 pF for a zero-bias RC time constant of 1 msec.

The blackbody responsivity, relative spectral response and noise of several diodes at 77°K were measured as a function of frequency and background. Since the PbTe thin films are on transparent substrate ( $\text{BaF}_2$ ) and are on the order of 7  $\mu\text{m}$  thick, these measurements were made with the signal and background radiation incident first from the p-type side of the junction through the  $\text{BaF}_2$  substrate and then on the  $\text{Sb}^+$  implanted n-type side.

The detectivity obtained from these measurements as a function of wavelength for a typical diode in reduced background with the signal incident on the  $\text{Sb}^+$  implanted n-type side is shown in Fig. I-12. The peak detectivity occurs at 5.3  $\mu\text{m}$  and is  $4.5 \times 10^{11} \text{ cmHz}^{1/2}/\text{W}$  at 200 Hz with the 77°K background. The peak quantum efficiency is 55 percent.

The detectivity as a function of wavelength with the signal incident on the p-type side of the diode through the  $\text{BaF}_2$  substrate is shown in Fig. I-13. The peak detectivity in this case occurs at 5.5  $\mu\text{m}$  and is  $4.4 \times 10^{11} \text{ cmHz}^{1/2}/\text{W}$  at 200 Hz with the 77°K background. The peak quantum efficiency is 51 percent. Note that the detectivity is much more sharply peaked when the signal is incident on the p-type side of the PbTe.

The measured detectivity in both cases was essentially constant from 100 to 800 Hz, the frequency range of measurement. There was a slight rolloff at the higher frequencies, since at these frequencies amplifier noise is becoming a significant fraction of the total noise due to the RC rolloff in diode noise. (The diode responsivity is also decreasing due to the RC time constant.) The measured peak detectivity in both cases, however, is only about 50 percent of the calculated Johnson noise limited detectivity. The reason for this discrepancy has not been determined at the present time.

On comparing these initial results with results obtained on  $\text{Sb}^+$  implanted PbTe diodes fabricated in bulk crystals with p-type carrier concentrations ranging from 3 to  $7 \times 10^{18} \text{ cm}^{-3}$  (Ref. 3), we observed the following. The bulk PbTe diodes had zero-bias resistances about an order of magnitude higher than those measured on these thin film PbTe diodes. The bulk PbTe diodes had measured peak detectivities in reduced background of  $1.6 \times 10^{12} \text{ cmHz}^{1/2}/\text{W}$ , which were limited by amplifier noise. This is about 3.5 times higher than the peak detectivities measured

## Section I

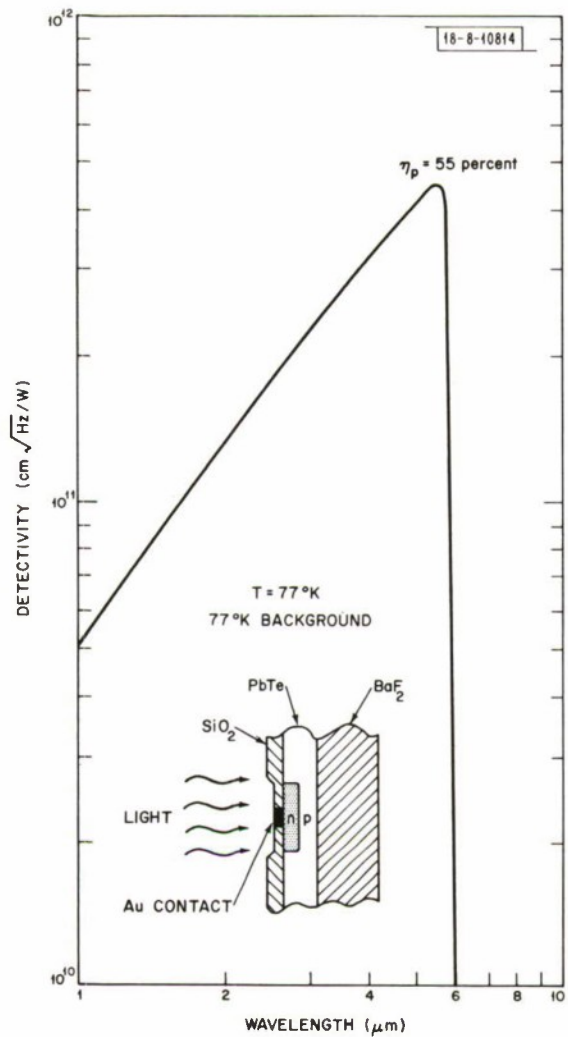


Fig. I-12. Detectivity as a function of wavelength of a 15-mil-square epitaxial PbTe diode with the signal incident on the  $\text{Sb}^+$  implanted n-type side.

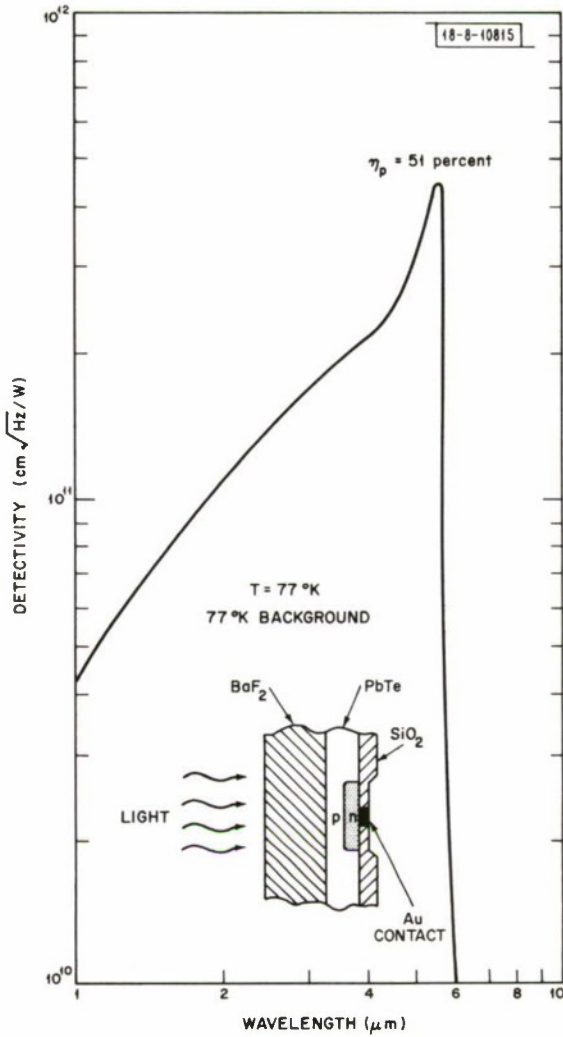


Fig. I-13. Detectivity as a function of wavelength of a 15-mil-square epitaxial PbTe diode with the signal incident on the p-type side through the  $\text{BaF}_2$  substrate.

on the PbTe thin film diodes. It is possible that these differences are primarily due to substrate carrier concentration differences. The diodes fabricated in the film epitaxial PbTe had a peak detectivity which occurred at 5.3  $\mu\text{m}$  (with the signal incident on the Sb<sup>+</sup> implanted n-type side). The diodes fabricated in the bulk grown PbTe crystals showed a peak detectivity at about 4.4  $\mu\text{m}$  (with the peak shifting to slightly shorter wavelengths as the carrier concentration was increased from 3 to  $7 \times 10^{18} \text{ cm}^{-3}$ ) with a very soft rolloff at longer wavelengths.<sup>3</sup> Although the reason for this discrepancy is not completely understood, it should be noted that the bulk crystals have a p-type carrier concentration about two orders of magnitude higher than the PbTe thin films. If most of the absorption is taking place in the p-type material, band filling in the bulk p-type material ( $p \geq 3 \times 10^{18} \text{ cm}^{-3}$ ) could explain this wavelength shift in the peak detectivity.

J. P. Donnelly  
A. G. Foyt

#### D. THERMAL PROPERTIES OF $\text{PbS}_{1-x}\text{Se}_x$ DIODE LASERS

The frequency tuning characteristics of  $\text{PbS}_{1-x}\text{Se}_x$  diode lasers<sup>12</sup> emitting near 5.2- $\mu\text{m}$  wavelength have been investigated under a variety of operating conditions. Since the laser frequency shift is caused by heating of the active region due to the bias current, a study of the current tuning is useful in evaluating the role of various diode parameters in determining the temperature of this region under both steady-state and transient conditions.

##### 1. Current-Tuning with DC and Small-Signal AC

Sb<sup>+</sup> ion implanted  $\text{PbS}_{0.62}\text{Se}_{0.38}$  diode lasers have been examined both for DC tuning rate and small signal AC tuning rate, while operating CW. The laser heat sink was maintained at  $\sim 13^\circ\text{K}$ , and an electronically scannable confocal Fabry-Perot interferometer<sup>13</sup> (FPI) was used to determine the shift in laser frequency.<sup>14</sup> The transmission characteristic of the FPI used here was a series of windows  $\sim 40$  MHz wide, equally spaced at intervals of 1500 MHz ( $0.05 \text{ cm}^{-1}$ ). Because the FPI aliased frequency separations greater than 1.5 GHz, a grating spectrometer was first used to determine the gross spacing between laser modes ( $\sim 44$  GHz for these lasers).

The DC tuning rate ( $d\nu/di$ ) was determined by slowly sweeping the diode current  $i$  while holding the FPI mirror separation fixed and measuring the current change necessary to shift the output by 1.5 GHz. Since the grating spectrometer was not used as a prefilter, all modes were folded into a characteristic pattern with a periodicity of 1.5 GHz. For a diode with a 0.06-ohm forward resistance (diode A) the DC tuning rate ranged from 83 MHz/mA at 200 mA bias to 190 MHz/mA at 1000 mA bias. A higher threshold device with a 0.19-ohm forward resistance, and thus increased heating, had a tuning rate of 500 MHz/mA at 1000 mA bias. The maximum continuous tuning range for a single mode in diode B was 100 GHz, and was covered by sweeping the current from 600 to 1000 mA.

To further characterize the thermal behavior, a small (1 to 10 mA peak-to-peak) sinusoidal current was superimposed on the DC bias in order to observe the frequency response of the tuning. Figure I-14 illustrates the transmission spectrum of the scanned FPI for diode A biased at 650 mA, first with no modulation, then with 10 mA 100 kHz modulation, and finally with 10 mA 100 Hz modulation. When these data were recorded, the alignment of the FPI and the laser beam was sufficiently precise to obtain mode-matching, for which case the FPI maintains a 40-MHz resolution, but doubles the free spectral range. Thus, the spectra in Fig. I-14 have a pattern

Section I

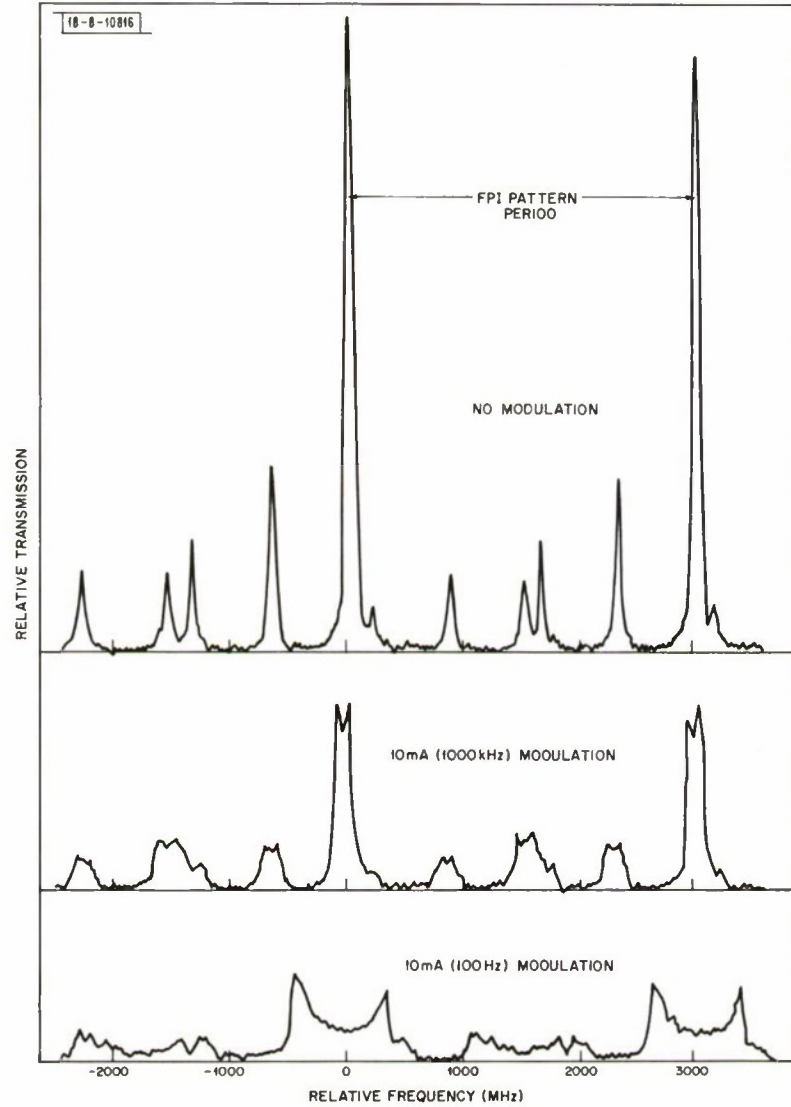


Fig. I-14. Transmission spectra of scanned FPI for diode laser operating CW at 650-mA bias for various modulation levels. Pattern periodicity is 3000 MHz.

periodicity of 3 GHz. The shape of the broadened modes observed is caused by the sinusoidal time-variation of the modulation current. The lower frequency modulation is seen to tune the output through 720 MHz, appreciably more than the 100-MHz tuning at the higher frequency.

Derivative plots of the data in Fig. I-14 were made by detecting the laser output at the modulation frequency, and these derivative spectra were used to accurately measure the shift in laser frequency. Since for small AC currents the modulation depth of the laser frequency was found to be proportional to the amplitude of the AC current (as expected), the "AC tuning rate" can be defined as  $\Delta\nu/dI = \Delta\nu/\Delta I_p$ , where  $I_p$  is the peak-to-peak amplitude of the AC current. Figure I-15 shows the tuning rate at 650-mA bias as a function of modulation frequency for diodes A and B. For each diode we can distinguish three regions of interest: (a) the DC region, (b) a low frequency AC region ( $f < 10$  Hz), and (c) the high frequency region ( $f > 5000$  Hz).

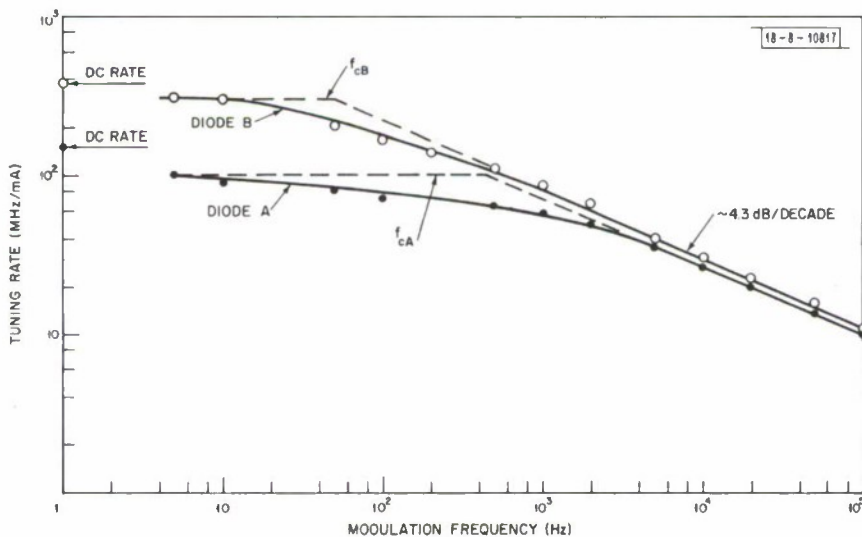


Fig. I-15. Tuning rate for two diode lasers operating CW at 650-mA bias for various modulation frequencies. Forward resistance was 0.06 ohm for diode A and 0.19 ohm for diode B.

The data can be interpreted with the aid of the equivalent circuit model for the heat flow in the diode laser shown in Fig. I-16. Most of the heat is generated in the active region of the forward biased p-n junction, since the external quantum efficiency is less than 10 percent, and at the contact to the p-region, which has a higher electrical resistance than the contact to the n-region. The power input due to these sources is given by  $Q_1 = i^2 r_1$  and  $Q_j = iV_g$ , where  $i$  is the diode current,  $r_1$  the resistance of contact 1 and  $V_g$  is the junction voltage, which is assumed to be equal to the barrier voltage of 0.24 V under forward bias. The bulk of the diode is modeled as a distributed thermal network consisting of per unit length thermal resistances  $r$  and capacitances  $c$ . The thermal resistance between the n region and the Cu heat sink is represented by  $R_2$ , and the Cu heat sink is represented by a lumped thermal resistance  $R_s$  and a capacitance  $C_s$ . The heat at the junction is actually generated throughout the active region which extends into the p-type bulk approximately as far as the carrier diffusion length, which we estimate to be 20 to 30  $\mu\text{m}$ . Since this region, combined with the 0.2- $\mu\text{m}$  implanted n region, is small

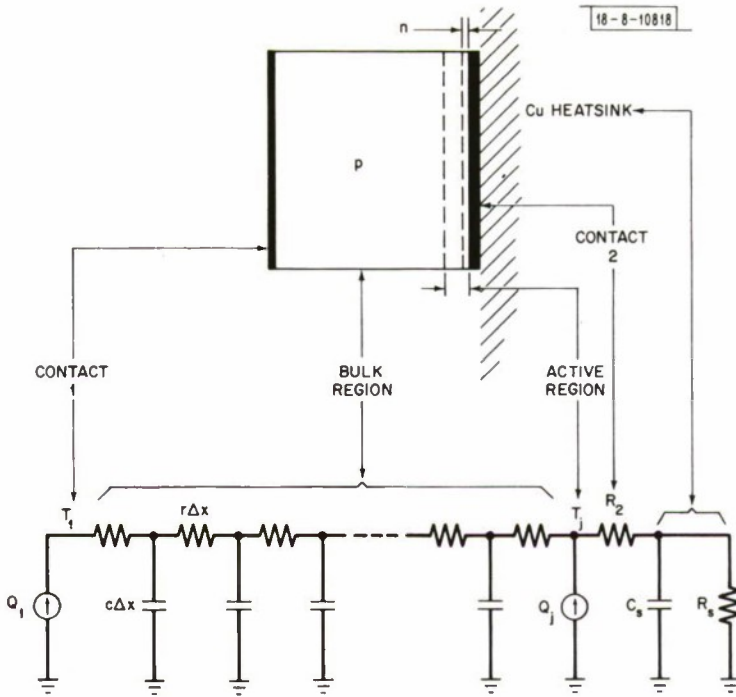


Fig. I-16. Equivalent circuit for heat flow in diode laser.

compared with the total thickness of 200  $\mu\text{m}$  for the diode, the junction heat is assumed to be a lumped source  $Q_j$  as indicated in Fig. I-16. The properties of the laser emission are determined by the temperature  $T_j$ . (The temperatures are measured with reference to the helium bath.) The tuning rate  $d\nu/di$  will be assumed to be proportional to  $dT_j/di$  at a given current level.

In the DC limit, the junction temperature is given by

$$T_j = (Q_1 + Q_j)(R_2 + R_s) = (i^2 r_1 + i V_g)(R_2 + R_s)$$

$$\frac{d\nu}{di} = k \frac{dT_j}{di} = k(2ir_1 + V_g)(R_2 + R_s) \quad (\text{I-1})$$

In the low frequency ( $f < 10$  Hz) limit, the large heat capacity of the heat sink is an equivalent short circuit and the tuning rate is given by

$$\frac{d\nu}{di} = k(2ir_1 + V_g) R_2$$

For higher frequencies, the distributed circuit has to be considered. It can be shown that in this range

$$T_j = \frac{Q_1 + Q_j \cosh(j\omega RC)^{1/2}}{\frac{1}{R_2} \cosh(j\omega RC)^{1/2} + (\frac{j\omega C}{R})^{1/2} \sinh(j\omega RC)^{1/2}} \quad (\text{I-2})$$

where  $R = rd$  and  $C = cd$  are the total thermal resistance and capacitance, respectively, for the diode with a bulk thickness  $d$ . Expressed in terms of the thermal conductivity  $k_1$  and heat

capacity  $e_p$  of the bulk,  $R = d/k_1 A$  and  $c = e_p Ad$ . In the high-frequency limit the tuning rate is given by

$$\frac{d\nu}{di} = k \frac{V_g}{A} \left( \frac{1}{j\omega k_1 e_p} \right)^{1/2} . \quad (I-3)$$

A cutoff frequency  $f_e$  can be defined as the intercept of the low frequency limit and the high frequency limit, i.e.,

$$f_e = \frac{V_g^2}{R_2^2 (2r_1 i + V_g)^2 2\pi A^2 k_1 e_p} . \quad (I-4)$$

In the high-frequency limit, the tuning rate according to Eq. (I-3) should vary as  $1/f^{1/2}$ , or 5 dB/decade. This can be compared with the experimentally observed 4.3 dB/decade variation for both diodes in Fig. I-15.

In analyzing the data, a complication arises because the rate of change of laser frequency increases with temperature,<sup>15</sup> i.e.,  $k$  is temperature dependent. Since diode B is expected to be at a higher temperature than diode A, because of a larger heat input in diode B (240 vs 185 mW), we expect that  $k_B > k_A$ . The ratio  $k_A/k_B$  can be estimated with the aid of Eq. (I-3) by comparing the high frequency tuning rates of A and B in Fig. I-15, assuming that the thermal conductivity and the heat capacity of the diode bulk is the same in both diodes. Under those conditions a simple ratioing gives  $k_A/k_B = 0.71$ .

Using the DC and the  $f = 5$  Hz tuning rates, we can then solve for relative values of  $k_A R_2$  and  $k_A R_s$  for the two diodes using Eqs. (I-1) and (I-2). From Table I-2 we note that the thermal resistance of the heat sink  $k_A R_s$  differs by about 20 percent for the two diodes, whereas the resistance of the interface to the heat sink normalized with respect to the area of the contact  $k_A R_2 A$  is about two times higher for diode B than for diode A. The ratio of the experimental cutoff frequencies  $f_{eA}/f_{eB}$  is 8.6, compared with the calculated value of 7.8 using Eq. (I-4), i.e., a satisfactory agreement.

From these results, it is apparent that both the junction temperature and the DC and low frequency tuning rates are strongly dependent on the contact resistance  $r_1$  and the thermal resistance of the mount  $R_2$ , but they do not depend on the thickness of the bulk region in the present model. A very significant improvement would result from separately heatsinking contact 1. The frequency cutoff is strongly dependent on  $R_2$ ,  $r_1$  and the junction area  $A$ . In the high frequency limit, which corresponds to adiabatic heating, the tuning rate depends only on the bulk parameters.

## 2. Pulsed Operation

An effort was also made to observe frequency chirp in pulsed operation using the FPI, but during the 1-μsec excitation pulses used, the modes shifted completely through the 1.5-GHz free spectral range; hence, only a lower bound of  $\gtrsim 0.05 \text{ cm}^{-1}/\mu\text{sec}$  could be placed on the chirp of the Sb<sup>+</sup> implanted lasers. The pulsed chirp has been evaluated for a diffused junction PbS<sub>0.62</sub>Se<sub>0.38</sub> laser by employing time resolved spectroscopy.

To examine the chirp in large signal pulsed operation we have employed a boxcar integrator with a small (100-nsec) gate width to probe a laser's spectral output during the moderately long

TABLE I-2  
PARAMETERS FOR  $\text{PbS}_{1-x}\text{Se}_x$  DIODE LASERS

	Diode A	Diode B
$A (\text{cm}^2)$	$3.6 \times 10^{-4}$	$4.6 \times 10^{-4}$
$d (\text{cm})$	$2 \times 10^{-2}$	$2 \times 10^{-2}$
$r_1 (\text{ohm})$	0.06	0.19
$Q_1 (\text{mW})$	25	80
$Q_j (\text{mW})$	160	160
$\frac{d\nu}{di} \Big _{f=0} (\text{MHz}/\text{mA})$	150	380
$\frac{d\nu}{di} \Big _{f=5 \text{ Hz}} (\text{MHz}/\text{mA})$	100	300
$k_A R_s (\text{Hz}/\text{W})$	0.16	0.13
$k_A R_2 (\text{Hz}/\text{W})$	0.31	0.44
$k_A R_2 A (\text{Hz cm}^2/\text{W})$	$1.1 \times 10^{-4}$	$2 \times 10^{-4}$
$f_c (\text{Hz})$	450	52

(6- $\mu$ sec) current pulse. A diffused junction  $\text{PbS}_{1-x}\text{Se}_x$  diode was operated with a 6- $\mu$ sec, 5-A pulse. A 100-nsec gate was set at 1- $\mu$ sec intervals from the beginning of the pulse and the spectra obtained by scanning a grating monochromator at each step. The modes observed in the diode emission shift to higher energy and change relative strength with time into the current pulse. An average chirp rate of 5.4 GHz/ $\mu$ sec is observed. This is in agreement with the lower bound obtained with the FPI for implanted lasers.

The absorption linewidth of a gas at atmospheric pressure is typically 5 GHz. Thus, with the present device, sufficient resolution could be achieved with pulses of 100 nsec, or shorter. In pollution monitoring, two alternate pulse schemes could be used: (a) the laser could be excited with 100-nsec pulses and independently temperature-tune the laser mode to scan through an absorption line of the gas, or (b) current pulses several  $\mu$ sec long could be applied, making use of the chirp as a built-in tuning mechanism. A detector with a 100-nsec gate scanned along the interval of the drive pulse could then be used to analyze the absorption spectrum.

Assuming adiabatic conditions during the pulse and an external quantum efficiency smaller than 10 percent (about 1 percent is typical for state-of-the-art lasers) the chirp rate can be simply calculated if we know the power input to the active region, the heat capacity, the volume of the active region, and the rate of change of the index of refraction with temperature. Except for the width of the active region, which has not been measured in these lasers, satisfactory estimates

can be made of these parameters from earlier measurements on lead-salt lasers and from known heat capacity values.<sup>16</sup> Using the available parameters, we find that 5.4-GHz/ $\mu$ sec chirp corresponds to a 40- $\mu$ m-wide active region. Active regions of approximately this width have been measured for  $Pb_{1-x}Sn_xTe$  lasers at 10  $\mu$ m.

At 77°K the heat capacity is estimated to be about eight times larger than at 15°K (Ref. 16) (the approximate temperature for the heatsink-mounted laser in the above experiment), but the rate of change of the index of refraction with temperature is expected to be about three times larger at 77°K. Thus, the combined effect of these two parameters would be to reduce the chirp by a factor of 2.5. However, the temperature dependence of the width of the active region has not been determined in these lasers; hence, an accurate estimate of the chirp at 77°K cannot be made at this time.

For a  $Pb_{1-x}Sn_xTe$  laser at 77°K a chirp of 60 GHz/ $\mu$ sec has been previously measured for an 8-A pulse.<sup>17</sup> This suggests that the active region is narrower at 77°K than at 15°K. A chirp rate of this magnitude would require a 10-nsec driving pulse. The alternate approach is to reduce the chirp by the use of an external cavity which should be capable of reducing the chirp by as much as a factor of 60. Measurements are in progress to accurately determine the chirp in  $PbS_{1-x}Se_x$  lasers at 77°K.

J. M. Mikkelson	A. R. Calawa
E. J. Johnson	J. P. Donnelly
R. W. Ralston	T. C. Harman
J. N. Walpole	I. Melngailis

REFERENCES

1. Solid State Research Report, Lincoln Laboratory, M.I.T. (1971:4), p. 1, DDC AD-736501.
2. Solid State Research Report, Lincoln Laboratory, M.I.T. (1972:1), p. 1, DDC AD-740874.
3. Solid State Research Report, Lincoln Laboratory, M.I.T. (1972:3), p. 1, DDC AD-752556.
4. Ref. 3, p. 11.
5. L.J. van der Pauw, Phillips Res. Rept. 13, 1 (1958).
6. J.P. Donnelly, T.C. Harman and A.G. Foyt, Appl. Phys. Letters 18, 259 (1971), DDC AD-728193.
7. A.R. Riben and D.L. Feucht, Solid State Electronics 9, 1055 (1966).
8. R.T. Bate, D.L. Carter and J.S. Wrobel, Phys. Rev. Letters 25, 159 (1970).
9. R.T. Bate, D.L. Carter and J.S. Wrobel, Proc. of the Tenth International Conference on the Physics of Semiconductors, Cambridge, Massachusetts, 17-21 August 1971.
10. H. Holloway, E.M. Logothetis and E. Wilkes, J. Appl. Phys. 41, 3543 (1970).
11. E.M. Logothetis, H. Holloway, A.J. Varga and E. Wilkes, Appl. Phys. Letters 19, 318 (1971).
12. Solid State Research Report, Lincoln Laboratory, M.I.T. (1971:2), p. 5, DDC AD-732923.
13. M. Hercher, Appl. Opt. 7, 951 (1968).
14. Ref. 1, p. 17.
15. Solid State Research Report, Lincoln Laboratory, M.I.T. (1971:3), p. 15, DDC AD-731547.
16. D.H. Parkinson and J.E. Quarrington, Proc. Phys. Soc. (London), A67:569 (1954).
17. Optics Research Report, Lincoln Laboratory, M.I.T. (1970:3), p. 43, DDC AD-882617.

## II. QUANTUM ELECTRONICS

### A. EFFICIENT OPTICALLY PUMPED InP AND $\text{In}_x\text{Ga}_{1-x}\text{As}$ LASERS

By optically pumping room temperature InP and  $\text{In}_x\text{Ga}_{1-x}\text{As}$ , we have obtained greater than 1-W output pulses from active regions  $\sim 20 \mu\text{m}$  wide and  $\sim 5$  to  $10 \mu\text{m}$  deep. We note that this is comparable to the typical data for high level operation of GaAs diodes. At these power levels, total power conversion efficiencies of 3 to 4 percent were obtained.

The InP samples were obtained from Czochralski-grown material with the following characteristics:  $n_{300} \approx 1.2$  to  $2.3 \times 10^{15}/\text{cm}^3$ ,  $\mu_{300} \approx 3200 \text{ cm}^2/\text{V sec}$  and  $\rho_{300} \approx 1.5 \text{ ohm-cm}$ . The  $\text{In}_x\text{Ga}_{1-x}\text{As}$  samples were obtained from material whose characteristics have been described elsewhere.<sup>1</sup> Experimentally, the equipment and sample preparation techniques are similar to those presented in Ref. 1, except in this case we use as the excitation source the output of a tunable parametric oscillator. The oscillator emitted light pulses whose wavelength could be varied over the range necessary for these experiments, in this case from 9000 to 9600 Å.

In Fig. II-1 we show typical emission spectra for the InP and  $\text{In}_x\text{Ga}_{1-x}\text{As}$  samples excited well above threshold. The emission spectrum of the InP was obtained with the pump wavelength at 9150 Å and at an incident power level of 60 W. The corresponding figures for the  $\text{In}_{0.06}\text{Ga}_{0.94}\text{As}$  are 9350 Å and 45 W. In both cases, the difference in energy between the pump radiation and sample laser light is  $\sim 26$  meV, or about kT, at room temperature. Compared with the normal case in optical pumping where  $h\nu_{\text{pump}} - h\nu_{\text{sample}} \gg kT$ , by using pump light this close to the semiconductor band edge we effectively move the excitation away from the

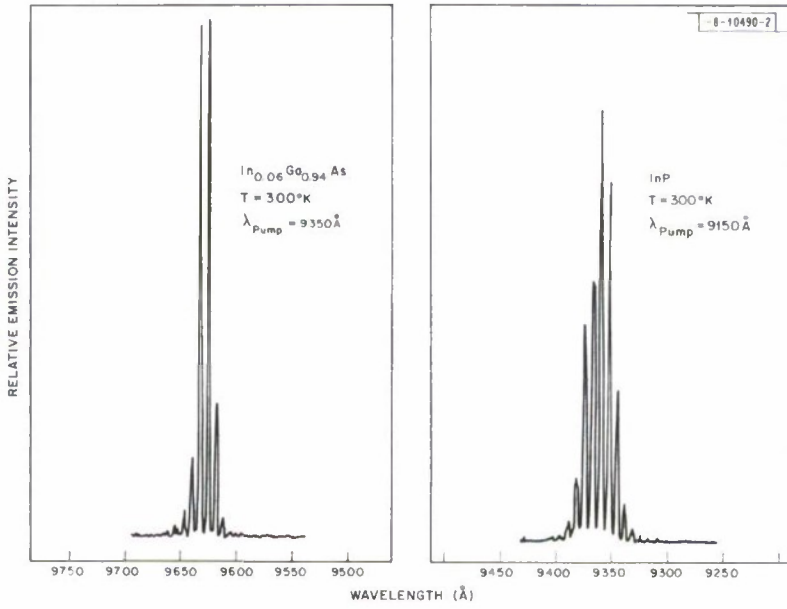


Fig. II-1. Lasing emission spectra from InP (right) and  $\text{In}_x\text{Ga}_{1-x}\text{As}$  (left) obtained by optical pumping at room temperature.

## Section II

surface of the sample and into the bulk. This has two beneficial effects. First, the surface recombination captures fewer of the excited carriers and thus the excitation creates a lower, but more spatially uniform, excess carrier density. Second, any heating present is spread over a much larger volume. Of course, the lower excess carrier density demands a higher pump power to achieve lasing, and this effect is well established experimentally.<sup>2</sup> Changing the excitation wavelength to shorter values (i.e., increasing the difference  $h\nu_{\text{pump}} - h\nu_{\text{sample}} > 0$ ) changes the waveguide properties of the portion of the sample being excited, as well as the degree of inversion in the excited region.<sup>2</sup>

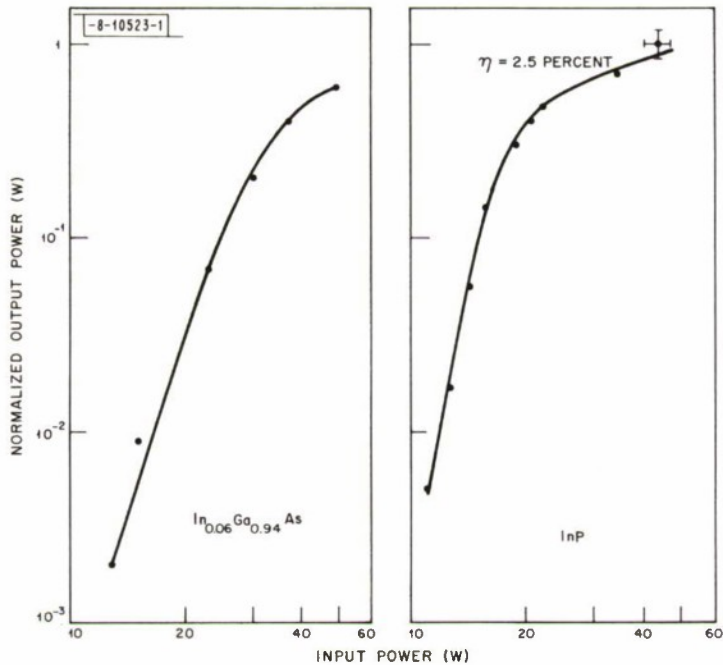


Fig. II-2. Normalized output power from InP (right) and  $\text{In}_x\text{Ga}_{1-x}\text{As}$  (left) as a function of pump input power (see text for a discussion of the normalization). Error bars are shown on uppermost point of InP curve.

Figure II-2 shows the normalized sample output power as a function of input pump power. This normalization accounts for the reflected pump light and the sample light emitted from both cavity faces. The peak measured power out of one emitting face of the InP was 0.35 W, while from the  $\text{In}_{0.06}\text{Ga}_{0.94}\text{As}$ , 0.21 W was obtained. At these power levels the normalized total power conversion efficiencies, that is, the ratios of sample emitted power to pump power absorbed, are roughly 2.5 and 1.2 percent, respectively. The results presented in Fig. II-2 are typical of the many samples used. However, we have obtained even higher output powers and better efficiencies on a few select samples. For example, from the InP we have measured 1.15 W emitted from one cleaved face at a normalized power conversion efficiency of 4 percent. The corresponding numbers for the best  $\text{In}_x\text{Ga}_{1-x}\text{As}$  are 0.86 W and 3 percent efficiency.

To compute the output power density at the emitting (cleaved) face, we need to know both the size of the focused incident beam and the effective depth of inversion. The line image of the focused beam we estimate to be 20  $\mu\text{m}$ . This estimate slightly exceeds the theoretical diffraction

limit and is indirectly confirmed by a measurement of the width of damage incurred by the samples under much higher excitation conditions. Since the excess carrier lifetime under the conditions of stimulated emission are expected to be short,<sup>3</sup> we may use the 20  $\mu\text{m}$  width with confidence. From previous measurements of the far field pattern, we estimate the effective depth of inversion to be more than 5, but less than 10  $\mu\text{m}$ . Using the conservative number (10  $\mu\text{m}$ ) the output power densities have reached  $5 \times 10^5 \text{ W/cm}^2$  for both types of samples. We emphasize that these figures are high; the catastrophic failure level for many uncoated GaAs diodes is  $\sim 10^6 \text{ W/cm}^2$  (Ref. 4). Since this latter figure applies to active regions  $\sim 2 \mu\text{m}$  thick and to an entirely different geometry, a direct comparison of the two power densities is difficult to make. Nevertheless, the measured output powers and efficiencies represent almost an order of magnitude increase over previous results.<sup>1</sup> This increase in efficiency, as well as the cleaner spectra (i.e., less chirping, narrower modes), we attribute solely to the use of a pump satisfying the relation  $h\nu_{\text{pump}} - h\nu_{\text{sample}} \approx kT$ .

J. A. Rossi  
S. R. Chinn

#### B. PRESSURE-TUNED GaAs DIODE LASERS FOR HIGH-RESOLUTION SPECTROSCOPY

The spectral characteristics of GaAs diode lasers have been studied over a pressure range from 0 to 7 kbars at a temperature of 77°K. The frequency of emission is known to tune almost linearly with pressure.<sup>5</sup> Typical longitudinal mode structure of a commercially available GaAs diode is shown in Fig. II-3. The mode pattern, threshold and intensity of emission are nearly independent of pressure. As a function of pressure, the longitudinal modes pull at a rate of

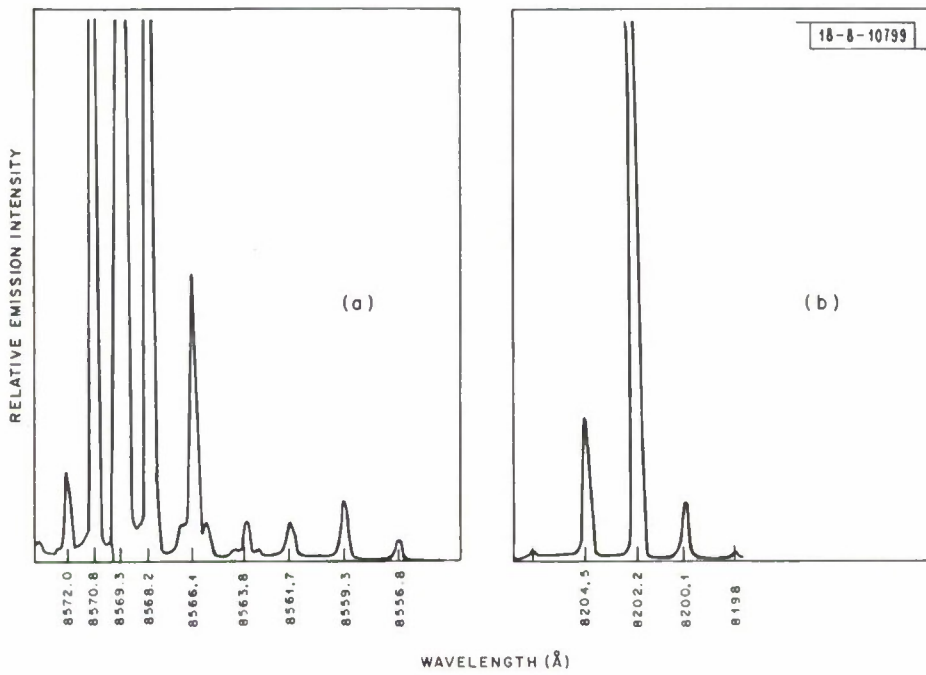


Fig. II-3. Spectrometer traces of longitudinal mode structure in GaAs diode laser under pressure: (a) 0 kbar; (b) 5.75 kbar.

## Section II

about one-third the spontaneous emission peak. The laser spectral pattern follows the spontaneous emission. Thus there is considerable mode hopping with frequency gaps of greater than 50 percent of the mode spacing.

The traces shown in Fig. II-3 are limited by the resolution of the spectrometer. The principal contributions to the longitudinal mode linewidths are from frequency chirp during the laser pulse and from transverse mode structure. These effects can be observed by transmitting a given longitudinal mode through a Fabry-Perot interferometer, as shown in Fig. II-4. The 10-GHz free spectral range of the interferometer is observed between any two equal sized peaks spaced by about 4  $\mu$ sec. Subsidiary peaks arise from other transverse modes. The total power in the longitudinal mode during the 8- $\mu$ sec pulse is shown in the background trace in Fig. II-4. Obviously, the multi-transverse mode nature of the emission is detrimental to the display of high resolution absorption spectra.

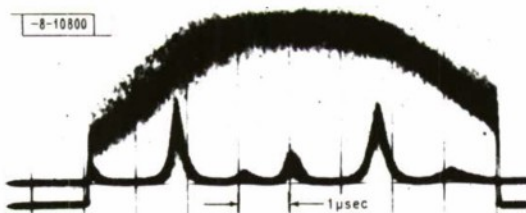


Fig. II-4. Interferometer trace of transverse mode structure in GaAs diode laser.

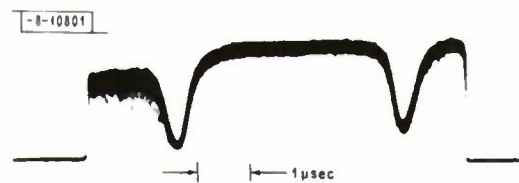


Fig. II-5. Absorption doublet in 8521  $\text{\AA}$  resonance line of  $\text{Cs}^{133}$  vapor by pressure tuned (0.5 kbar) GaAs diode laser spectroscopy.

Diodes with nearly single transverse mode behavior may be selected (two out of a stock of ten) to give the type of absorption spectrum illustrated in Fig. II-5. The laser (at about 0.5 kbar in this case) emission is passed through a 5-cm cell with saturated Cs vapor at 295°K. The doublet of spacing 9.2 GHz is caused by nuclear hyperfine interactions<sup>6</sup> in the ground state of the  $\text{Cs}^{133}$  resonance line at 8521  $\text{\AA}$ . The background is uniform except for the fuzziness caused by longitudinal mode competition. Broadening of the peaks is due primarily to the Doppler width (~400 MHz) and unresolved hyperfine interactions in the excited state (~500 MHz). The time resolution of 20 nsec for the 2.5-GHz/ $\mu$ sec chirp rate indicates an instrumental resolution of ~50 MHz.

The diodes are operated in a pulsed mode because of the 77°K temperature required in order to prevent the high pressure fluid, helium, from freezing. CW or lower chirp diodes would, of course, increase the experimental resolution. The diodes should have the lowest threshold possible in order to minimize chirp due to heating. Furthermore, diode fabrication and packaging must be compatible with the high pressure system. Both gradual and catastrophic failure of the diode lasers have been observed. Catastrophic failures usually occur during decompression, when pressure built up under the contacts explodes the header. Gradual deterioration may occur through contact and junction diffusion in the high pressure environment. However, this cause has not been conclusively proven, since diodes generally degrade with use under any conditions.

Pressure stability is also a prerequisite to pressure-tuned high resolution spectroscopy. Though details of the pressure vessel and apparatus will be discussed elsewhere, suffice it to say that leak-free operation is not trivial. The seals in our present system are very sporadic,

and the pressure vessel itself is subject to severe wear. Redesign of the pressure system is under active consideration in terms of both materials and sealing techniques.

A. S. Pine  
C. J. Glassbrenner  
J. A. Kafalas

### C. SPIN-FLIP RAMAN LINewidth MEASUREMENTS AND NONLINEAR PROCESSES IN InSb

We have continued our investigation of the spin-flip Raman process in InSb. A direct measurement of the Raman gain has been made by focusing two laser beams at frequencies  $\omega_1$  and  $\omega_2$  into a sample of n-type InSb in a magnetic field and varying the magnetic field through the spin-resonance condition,  $\omega_s = \omega_1 - \omega_2$ . If the laser beams are properly polarized ( $\hat{\epsilon}_1 \times \hat{\epsilon}_2 \perp \vec{H}$ , where the  $\hat{\epsilon}$ 's are the unit polarization vectors of the photons), there is gain at the Stokes frequency  $\omega_2$  corresponding to the pump frequency  $\omega_1$  and, concomitantly, loss at the pump frequency. By working at sufficiently low pump power levels, this technique allows a direct measurement of the spin-flip Raman lineshape. This lineshape plays an important role in determining the gain and tuning characteristics<sup>7</sup> of the spin-flip laser, as well as in controlling the frequency modulation and fast pulse generation properties of the spin-flip laser under the application of small electric fields.<sup>8</sup> Because the spin-flip linewidth is extremely narrow [less than 100 MHz ( $0.003 \text{ cm}^{-1}$ ) for some experimental conditions], this lineshape is not accessible by ordinary spectroscopic techniques.

The experimental arrangement is shown in Fig. II-6. The two laser beams are combined with a Ge beamsplitter, antireflection-coated on one side so that there is only one partially reflecting surface. It is important that the two beams be made as collinear as possible, since any component of the scattering wavevector,  $\vec{q} = \vec{k}_1 - \vec{k}_2$ , parallel to the magnetic field can give rise

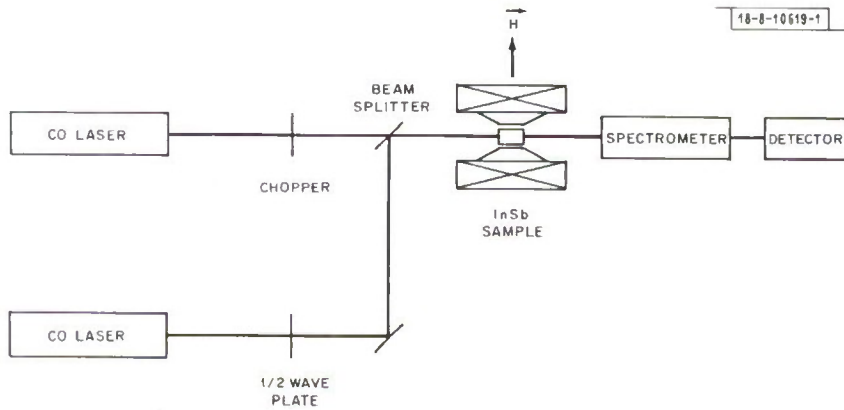


Fig. II-6. Experimental arrangement for measurement of nonlinear optical processes in InSb.

to substantial broadening of the observed lineshape.<sup>9</sup> In the present experiments, the angle between  $\vec{k}_1$  and  $\vec{k}_2$  was less than  $\frac{1}{4}^\circ$  inside the sample and, therefore, had a negligible effect on the lineshape. The sample was immersed in superfluid helium ( $T \sim 2^\circ\text{K}$ ) and placed in an electromagnet ( $H \lesssim 10 \text{ kG}$ ). The exit face of the sample was ground with a 5- $\mu\text{m}$  grit in order to diffusely scatter the laser beams and minimize cavity effects. The chopper was placed in the  $\omega_1$  laser

## Section II

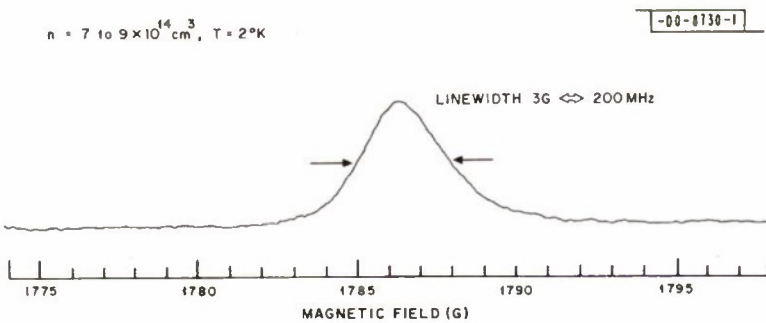


Fig. II-7. Lineshape of spin-flip Raman scattering ( $\omega_1 = 1868.1 \text{ cm}^{-1}$ ,  $\omega_2 = 1864.0 \text{ cm}^{-1}$ , T = 2°K, n =  $8 \times 10^{14} \text{ cm}^{-3}$ ).

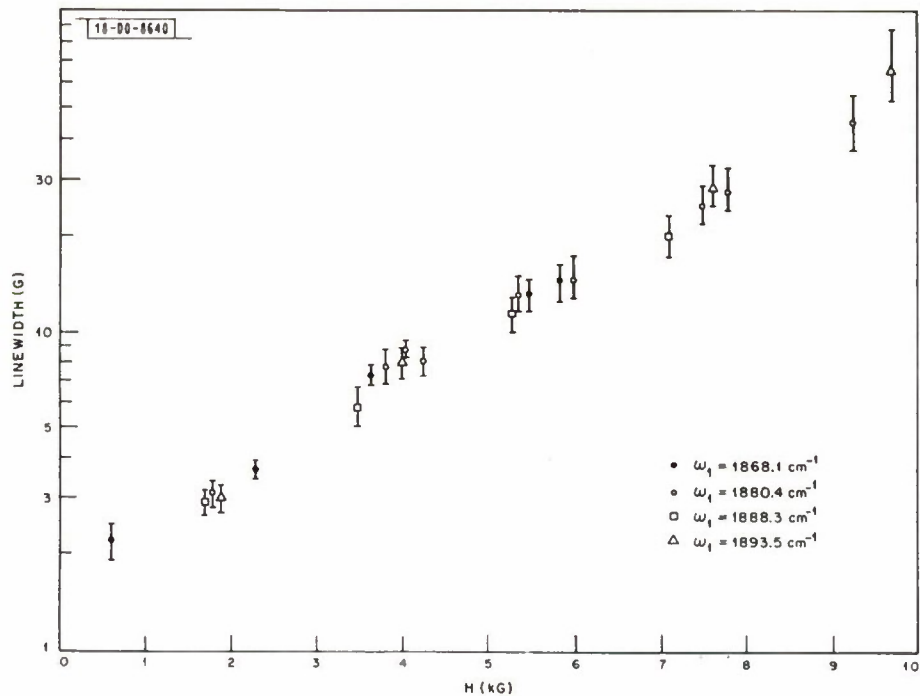


Fig. II-8. Variation of spin-flip Raman linewidth with magnetic field (T = 2°K, n =  $8 \times 10^{14} \text{ cm}^{-3}$ ).

beam and the gain was measured by synchronously detecting the transmitted power at  $\omega_2$ . This results in a signal proportional to  $\{\exp[g(H)l] - \beta\}$ , where  $g(H)$  is the spin-flip Raman gain which is proportional to the laser power at  $\omega_1$ ,  $l$  is the sample length and  $\beta$  is a field independent parameter somewhat less than unity, which indicates that there is a small amount of power at  $\omega_2$  modulated at the chopping frequency far away from the resonance condition due possibly to thermal effects. In the small signal regime, the signal is linearly related to the gain and hence the lineshape. The experiments reported here were carried out at two power levels of the pump radiation  $P_{\omega_1}$  and  $P_{\omega_1}/2$  to insure that they were in the linear regime.

The results of this experiment for a frequency difference  $\omega_1 - \omega_2 = 4.17 \text{ cm}^{-1}$  are shown in Fig. II-7. The observed lineshape is symmetric and has a full width at half height of 3 G, which corresponds to a frequency width of 200 MHz using the measured tuning rate of 67.5 MHz/G. The resolution is limited only by the frequency instabilities in the two lasers and is less than 1 MHz.

The variation in this linewidth as a function of magnetic field is shown in Fig. II-8. At all magnetic fields the lineshape was symmetric and approximately Lorentzian. Because these experiments were carried out so close to the interband resonance in InSb (the energy gap at zero field is approximately  $1888 \text{ cm}^{-1}$ ), the measurements were repeated for several values of  $\omega_1$ . As is indicated in Fig. II-8, variation of the pump photon energy had no effect on the linewidth to within experimental error.

For the sample electron density of  $\sim 8 \times 10^{14} \text{ cm}^{-3}$ , the quantum limit in which all the electrons are in the lowest Landau sub-level is reached for magnetic fields of approximately 5 kG. For magnetic fields of greater than 4 to 5 kG, nonparabolicity effects dominate the lineshape,<sup>9</sup> since excitations are possible from anywhere below the Fermi surface. As  $H$  is decreased, more Landau levels drop below the Fermi surface and the spin excitations become limited to initial states on the Fermi surface. Here, the nonparabolicity broadening mechanisms are not effective and the resultant lineshape is narrower and dominated by spin-relaxation processes. Thus, at the lowest magnetic field at which gain was measured in the present experiments,  $H = 600 \text{ G}$ , the first eight (up to  $n = 4$ ) Landau sub-levels are partially occupied at  $T = 0^\circ\text{K}$ . At these low fields, the present experiments should be comparable to previous microwave spin resonance measurements in InSb and, indeed, the linewidth of approximately 2 G at a magnetic field of 500 G is in substantial agreement, although somewhat broader than the previous measurements.<sup>10</sup> For magnetic fields higher than the 5 kG needed to reach the quantum limit, the electrons at  $T = 0^\circ\text{K}$  are being packed into lower and lower  $k_z$  states near the bottom of the conduction band, because of the increasing density of states. This would be reflected in a narrower linewidth. However, finite temperature effects set a limit on how low in the band the electrons can be packed, since states with energies up to several  $kT$  are occupied for  $kT \lesssim \epsilon_F$  (note  $kT/\epsilon_F \sim 0.8$  for  $T = 2^\circ\text{K}$  and  $H = 10 \text{ kG}$ ). In the limit in which the electron distribution is Maxwellian ( $kT/\epsilon_F \gg 1$ ), the linewidth is given by<sup>8,9</sup>

$$\Gamma \approx 2\tau_p \omega_{so}^2 (kT)^2 / \epsilon_g^2 \quad (\text{II-1})$$

where  $\tau_p$  is a time which characterizes processes that alter the  $k_z$  state-of-the-spin excitation,  $\omega_{so}$  is the spin frequency at the bottom of the band and  $\epsilon_g$  is the bandgap energy. In this limit, the linewidth is a strongly increasing function of  $H$ ,  $\Gamma \propto H^2$ . The details of the comparison between theory and experiment are presently being studied.

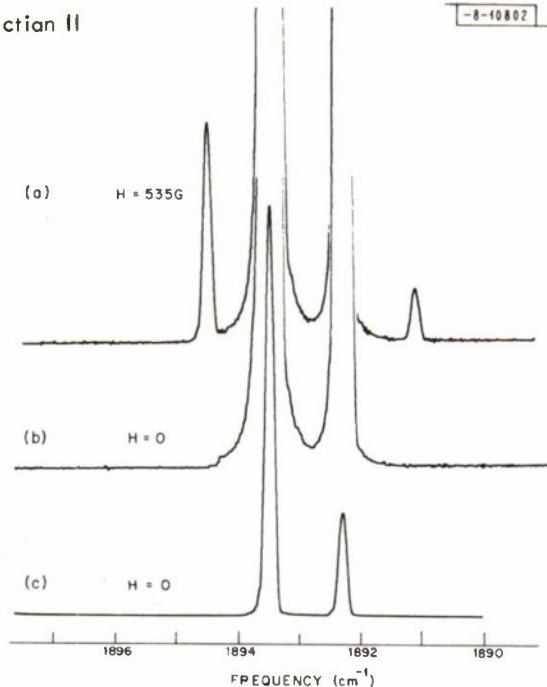


Fig. II-9. Spectrometer trace of output of an InSb sample: (a) on resonance  $H = 535$  G showing the three wave mixing processes  $\omega_3 = 2\omega_1 - \omega_2$  and  $\omega_4 = 2\omega_2 - \omega_1$ ; (b) similar to trace (a) with  $H = 0$  showing the absence of the three wave mixing; (c) as in (b) but lower gain to show relative powers  $P_{\omega_1}$  and  $P_{\omega_2}$ .

In addition to these gain measurements, this experimental configuration allows the study of several other interesting optical nonlinearities that arise from the spin-flip process. The results of a degenerate four-wave frequency mixing experiment are shown in Fig. II-9. In this experiment the two incident frequencies,  $\omega_1$  and  $\omega_2$ , are mixed to give a modulation of the InSb polarizability at frequency  $\omega_1 - \omega_2$  resulting in output waves at both  $\omega_3 = 2\omega_1 - \omega_2$  and  $\omega_4 = 2\omega_2 - \omega_1$ . This modulation of the polarizability results from the spin-flip process and is resonant for  $\omega_s = \omega_1 - \omega_2$ . The top trace is a spectrometer analysis of the transmitted power showing the two new frequencies  $\omega_3$  and  $\omega_4$ . The second trace is similar to the top one, but was taken at  $H = 0$  where there was no Raman nonlinearity and hence no frequency mixing. The bottom trace was again taken at  $H = 0$  at a lower gain level to show the relative intensities of  $P_{\omega_1}$  and  $P_{\omega_2}$ . This measurement was carried at a magnetic field of 535 G with a frequency separation  $\omega_1 - \omega_2 = 1.25 \text{ cm}^{-1}$  and in a sample of concentration  $n = 1 \times 10^{14} \text{ cm}^{-3}$ . There is a residual nonlinearity even at zero magnetic field in InSb due to the nonparabolicity of the conduction band. This nonlinearity is not evident in the data of Fig. II-9 because of the low electron concentration; however, in higher concentration samples it was possible to observe an interference between the resonant and nonresonant contributions to the third order nonlinear susceptibility. In addition, by properly adjusting the grating in one CO laser it was possible to generate two frequencies on adjacent laser transitions in one laser, say  $\omega_1$  and  $\omega'_1$ , separated by 1 to 2 cm. These lines could then be used to observe the nondegenerate four-wave mixing processes  $\omega_3 = \omega_1 - \omega_2 + \omega'_1$  and  $\omega_4 = \omega'_1 - \omega_2 + \omega_1$ , which allow the observation of the resonant nonlinearity for larger frequency shifts  $\omega_1 - \omega_2$  under phase matched conditions, since  $\omega_1 - \omega'_1$  is small.

S. R. J. Brueck  
A. Mooradian

## REFERENCES

1. J.A. Rossi, S.R. Chinn and A. Mooradian, *Appl. Phys. Letters* 20, 84 (1972), DDC AD-737941.
2. S.R. Chinn, J.A. Rossi, C.M. Wolfe and A. Mooradian, *IEEE Semiconductor Laser Conference*, Boston, Massachusetts, May 1972 (to be published in *IEEE J. Quantum Electron.*).
3. D.L. Keune, N. Holonyak, Jr., R.D. Burnham, D.R. Scifres, H.R. Zwicker, J.W. Burd, M.G. Crawford, D.L. Dickus and M.J. Fox, *J. Appl. Phys.* 42, 2048 (1971).
4. H. Kressel and H. Mierop, *J. Appl. Phys.* 38, 5419 (1967).
5. J. Feinleib, S.H. Groves, W. Paul and R. Zallen, *Phys. Rev.* 131, 2070 (1963).
6. U. Hochuli, P. Haldemann and S. Siahatgar, *J. Appl. Phys.* 40, 3374 (1969).
7. S.R.J. Brueck and A. Mooradian, *Appl. Phys. Letters* 18, 229 (1971), DDC AD-729611; Solid State Research Report, Lincoln Laboratory, M.I.T. (1972:2), p. 17, DDC AD-748836.
8. A. Mooradian, S.R.J. Brueck, E.J. Johnson and J.A. Rossi, *Appl. Phys. Letters* (to be published) and Solid State Research Report, Lincoln Laboratory, M.I.T. (1972:3), p. 25, DDC AD-752556.
9. S.R.J. Brueck and F.A. Blum, *Phys. Rev. Letters* 28, 1458 (1972), DDC AD-752954.
10. R.A. Isaacson, *Phys. Rev.* 169, 312 (1968); E.M. Gershenson, N.M. Pevin and M.S. Fogel'son, *Fizika Tverdogo Tela* 10, 2880 (1968) [English Translation Soviet Physics-Solid State 10, 2278 (1969)].

### III. MATERIALS RESEARCH

#### A. PSEUDOBINARY PHASE DIAGRAM AND EXISTENCE REGIONS FOR $\text{PbS}_{1-x}\text{Se}_x$

The 1V-VI compounds PbS and PbSe, both of which have the rocksalt structure, form a complete series of solid solutions. Currently the  $\text{PbS}_{1-x}\text{Se}_x$  alloys are of considerable interest as materials for the fabrication of tunable diode lasers with emission wavelengths at 4.2°K varying with composition from 4.3 μm for PbS to 8.6 μm for PbSe. We report here the results of two experimental studies on  $\text{PbS}_{1-x}\text{Se}_x$  properties related to the production of diode lasers.

In the first study we have re-determined the liquidus and solidus curves of the PbS-PbSe pseudobinary phase diagram, reported earlier by Simpson,<sup>1</sup> in order to establish the conditions of temperature and melt composition required to grow alloy single crystals of desired composition by the Bridgman method. The liquidus points were obtained by thermal analysis performed during cooling runs on samples sealed in fused-silica ampoules. The measured points and the smooth curve based on them are plotted in Fig. III-1, together with the liquidus curve reported by Simpson. Our melting points for PbS (1111°C) and PbSe (1082°C) agree to within 2°C with Simpson's, but at intermediate compositions our liquidus curve lies below his by as much as 5°C. The accuracy of our data ( $\pm 1^\circ\text{C}$ ) is sufficient to establish that the liquidus curve exhibits a minimum (at  $x = 0.73$  and 1076°C), as does the liquidus curve for the PbS-PbTe system.<sup>2</sup>

Solidus points in the pseudobinary phase diagram were obtained by measurements on a series of  $\text{PbS}_{1-x}\text{Se}_x$  ingots prepared by the Bridgman method from molten mixtures of PbS and PbSe. Electron microprobe analysis was used to determine the mole fraction of PbSe at the tip of each

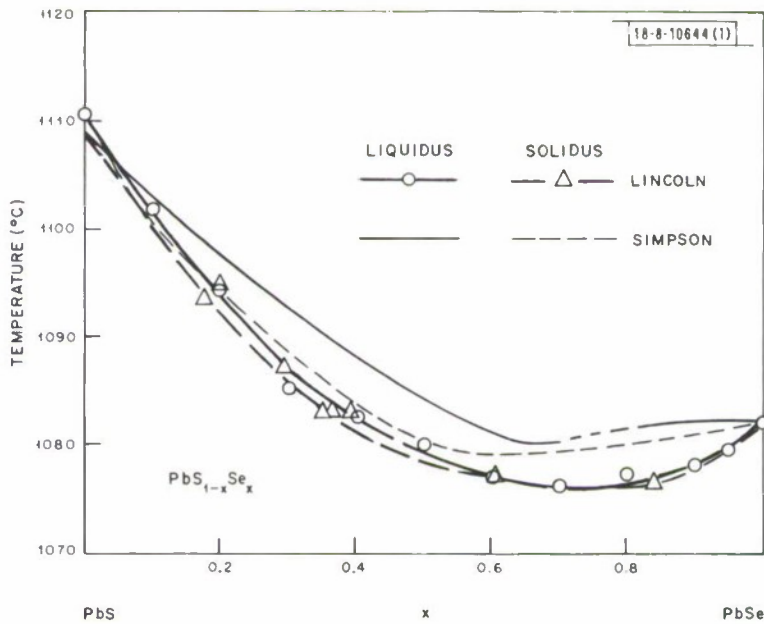


Fig. III-1. Phase diagram of pseudobinary PbS-PbSe system.

### Section III

ingot. Since it is the first portion of the ingot to freeze, the tip crystallizes from a melt whose composition (if homogeneous) is the nominal ingot composition given by the amounts of PbS and PbSe originally weighed out. If the tip freezes under equilibrium conditions, its composition is therefore the solidus composition that corresponds to the liquidus composition given by the nominal ingot composition. Each ingot therefore yields a point on the solidus curve determined by the measured tip composition and the temperature read off the liquidus curve for the nominal ingot composition.

The solidus points obtained for the  $\text{PbS}_{1-x}\text{Se}_x$  system and the smooth curve based on them are plotted in Fig. III-1, together with Simpson's solidus curve. Because the points are limited in number and exhibit some scatter, our solidus curve cannot be regarded as extremely accurate. Nevertheless, the data show clearly that there is very little separation between the solidus and liquidus curves. The closeness of the two curves is very advantageous for crystal growth from the melt because it reduces the composition change at the solid-liquid interface and therefore reduces the risk of constitutional supercooling. In addition, it reduces the composition gradients along the length of the ingot and within individual samples. For example, for an ingot with starting composition  $x = 0.20$ , the value of  $x$  increased from 0.175 at the tip to 0.244 at the top.

In our second experimental study on the  $\text{PbS}_{1-x}\text{Se}_x$  system, we determined the chalcogen-rich solidus lines for  $\text{PbS}_{0.62}\text{Se}_{0.38}$  and PbS. With these measurements, we have completed the determination of the existence regions for these two compositions, since the Pb-rich boundaries were found previously.<sup>3</sup> Chalcogen-rich samples of these materials are p-type, because the lattice defects associated with excess chalcogen are acceptors, and the hole concentration is determined by the excess chalcogen concentration. Therefore, the chalcogen solubility at a given temperature can be found by using Hall coefficient measurements to obtain the carrier concentration of samples which have been chalcogen-saturated at that temperature and then quenched.

In this study, chalcogen-saturated samples of  $\text{PbS}_{0.62}\text{Se}_{0.38}$  and PbS were prepared by a precipitation method similar to the one used in the earlier experiments to obtain Pb-saturated samples. This method can be used because the chalcogen solubility along the chalcogen-rich solidus lines, like the Pb solubility along the Pb-rich solidus lines, decreases with decreasing temperature. Because of this retrograde solubility, when a sample is chalcogen-saturated at one temperature and then cooled to a lower temperature, excess chalcogen tends to precipitate. If the annealing time is long enough for equilibrium to be reached, the concentration of excess chalcogen that remains dissolved will decrease to the value given by the solidus line.

The precipitation experiments were performed on single crystal samples cut from ingots grown by the Bridgman method. As-grown samples of  $\text{PbS}_{0.62}\text{Se}_{0.38}$ , which are n-type because they contain excess Pb, were first chalcogen-saturated at 900°C by annealing them in a sealed, fused-silica ampoule containing an ingot of  $\text{Pb}_{0.49}(\text{S}_{0.62}\text{Se}_{0.38})_{0.51}$ . Similarly, as-grown n-type PbS samples were S-saturated at 800°C by annealing with an ingot of  $\text{Pb}_{0.49}\text{S}_{0.51}$ . The p-type samples obtained in this way were annealed at temperatures between 800° and 300°C for periods from 16 hours to 30 days to reach equilibrium along the solidus line by precipitation. They were then quenched to room temperature, and the carrier concentrations were obtained by Hall coefficient measurements at 77°K.

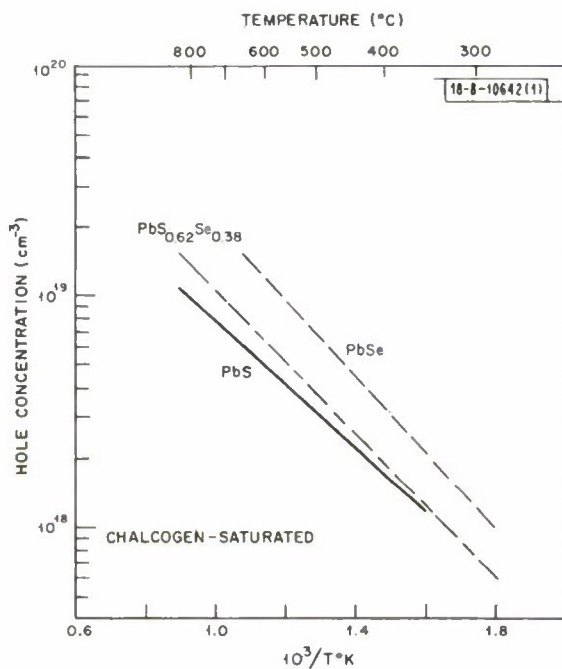


Fig. III-2. Chalcogen-rich solidus lines for PbS, PbSe and PbS<sub>0.62</sub>Se<sub>0.38</sub>.

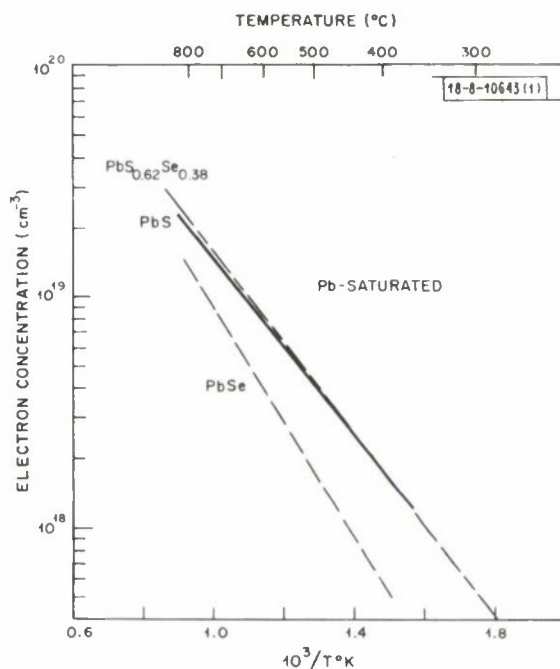


Fig. III-3. Pb-rich solidus lines for PbS, PbSe and PbS<sub>0.62</sub>Se<sub>0.38</sub>.

The chalcogen-rich solidus lines obtained by this procedure for PbS<sub>0.62</sub>Se<sub>0.38</sub> and PbS are shown in Fig. III-2, where the hole concentration measured at 77°K is plotted on a logarithmic scale against the reciprocal absolute annealing temperature. The chalcogen-rich solidus line for PbSe (Ref. 4) is also shown in Fig. III-2. For each of the three compositions, the results are given by a straight line. The Pb-rich solidus lines for these compositions are also straight lines on a log n vs 1/T plot, as shown in Fig. III-3 (Ref. 3). The parameters for the equations of the six straight lines are listed in Table III-1. Comparison of Figs. III-2 and III-3 shows that the existence regions of PbS and PbS<sub>0.62</sub>Se<sub>0.38</sub> are nearly symmetric with respect to the stoichiometric composition, while for PbSe the solubility of Se at a given temperature is significantly higher than that of Pb, and the solubility ratio increases with decreasing temperature.

A. J. Strauss  
T. C. Harman

#### B. ANALYSIS OF PbS<sub>1-x</sub>Se<sub>x</sub> ALLOYS BY X-RAY FLUORESCENCE

It has been demonstrated that the composition of PbS<sub>1-x</sub>Se<sub>x</sub> alloys can be conveniently and rapidly determined by using x-ray fluorescence to measure their Se content. Crystals with a flat, polished surface at least 6 mm in diameter were irradiated in air with a tungsten tube, and the intensity of the secondary SeK $\alpha$  x-radiation was measured using a LiF analyzer crystal and a scintillation counter with pulse height analyzers. To obtain a calibration curve, intensity data were collected for 9 crystals spanning the entire composition range and were plotted against the x values determined by electron microprobe analysis. The average error is equivalent to 1.75 percent of the value for x.

E. B. Owens

## Section III

Composition	$n = A \exp(-B/T) = A \exp(-C/kT)$		
	$A (\text{cm}^{-3})$	B (deg)	C (eV)
<b>Pb-saturated</b>			
PbS	$1.08 \times 10^{21}$	$4.34 \times 10^3$	0.37
$\text{PbS}_{0.62}\text{Se}_{0.38}$	$1.50 \times 10^{21}$	$4.54 \times 10^3$	0.39
PbSe	$2.75 \times 10^{21}$	$5.70 \times 10^3$	0.49
<b>Chalcogen-saturated</b>			
PbS	$1.95 \times 10^{20}$	$3.19 \times 10^3$	0.27
$\text{PbS}_{0.62}\text{Se}_{0.38}$	$3.91 \times 10^{20}$	$3.58 \times 10^3$	0.31
PbSe	$9.56 \times 10^{20}$	$3.80 \times 10^3$	0.33

## REFERENCES

1. D. R. Simpson, Econ. Geol. 59, 150 (1964).
2. M. S. Darrow, W. B. White and R. Roy, Trans. Met. Soc. AIME 236, 654 (1966).
3. Solid State Research Report, Lincoln Laboratory, M. I. T. (1972:1), p. 29, DDC AD-740874.
4. A. R. Calawa, T. C. Harman, M. Finn and P. Youtz, Trans. Met. Soc. AIME 242, 374 (1968), DDC AD-678986.

## IV. PHYSICS OF SOLIDS

### A. RARE-EARTH UPCONVERTING PHOSPHORS

In addition to the infrared-to-blue luminescence observed in the system  $\text{NaYF}_4$ : Yb, Tm, it was previously noted that the bulk of the anti-Stokes emission occurs at  $\lambda \approx 0.81 \mu\text{m}$ ,<sup>1</sup> while beyond the visible region, this emission wavelength is of interest since it matches the absorption band of YAG:Nd, as seen in Fig. IV-1.

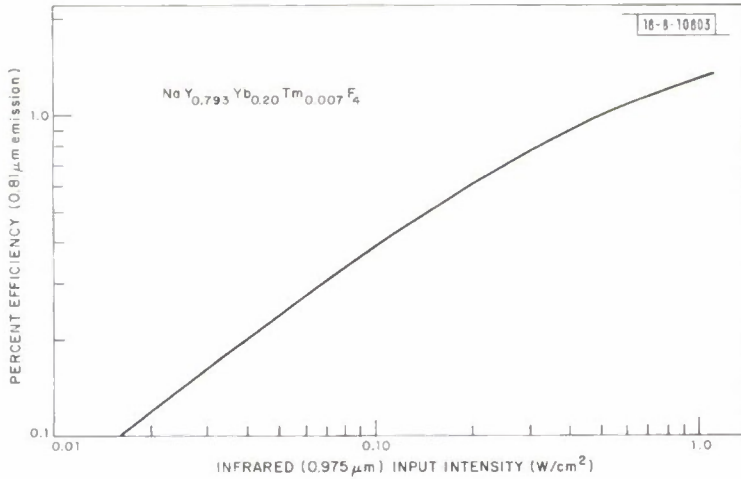


Fig. IV-1. Efficiency of  $0.81 \mu\text{m}$  emission from upconverting phosphor pumped at  $0.975 \mu\text{m}$ .

The upconversion efficiency of  $\text{NaY}_{0.793}\text{Yb}_{0.20}\text{Tm}_{0.007}\text{F}_4$ , as a function of excitation intensity, is shown in Fig. IV-2. The efficiency shown represents the radiant energy emitted around  $8100 \text{\AA}$  relative to the radiant energy striking the sample after passing through a  $9750\text{-\AA}$  filter with a  $150\text{-\AA}$  half-bandwidth. An efficiency of 1.4 percent is achieved with an input intensity of slightly over  $1 \text{ W/cm}^2$ . At this intensity level, saturation effects are playing a significant role and it appears that even with the higher intensities available from the most efficient diodes, the phosphor efficiency will not exceed 2 percent.

The temperature dependence of the  $0.81\text{-}\mu\text{m}$  emission at constant input intensity was studied between room temperature and  $100^\circ\text{K}$ . There is a small initial rise in output with decreasing temperature, reaching a broad maximum at  $225^\circ\text{K}$ . The overall change is slight, the most notable feature being the relative constancy of the output. (Over the  $125^\circ\text{K}$  interval from  $170^\circ$  to  $295^\circ\text{K}$ , the total output shifts by less than 7 percent.)

The rapid onset of saturation appears to make the combination of a GaAs:Si diode with upconverting phosphor less efficient for pumping a YAG:Nd laser than the use of a GaAsP diode.<sup>2</sup> Attempts to overcome this by the addition of direct pumping of the  $1.84\text{-}\mu\text{m}$  thulium level proved ineffective, presumably because of the low absorption cross section at this wavelength.

N. Menyuk  
K. Dwight  
J. W. Pierce

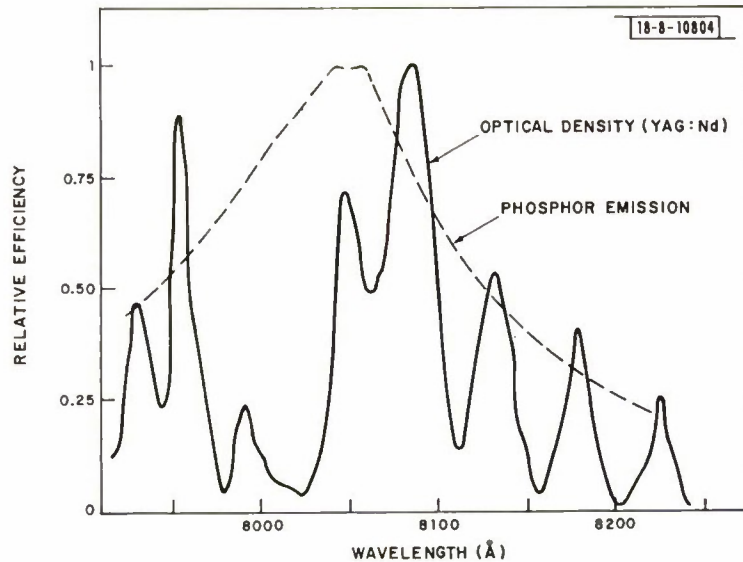


Fig. IV-2. Wavelength dependence of anti-Stokes emission from thulium  $^{3}F_4$  level compared with optical density of YAG:Nd (from Ref. 2).

### B. STABLE, HIGH YIELD SECONDARY-ELECTRON-EMITTING CATHODES

We are continuing our study of the secondary electron emission properties of non-insulating materials in an attempt to find materials with high yields at low primary electron energies that would be suitable for use as cold cathodes. The highest yields and lowest crossover voltages are generally found in insulating metal oxides, but surface charging renders them useless for cathode applications. We have previously found that  $\text{SnO}_2$ , which can be made partially conducting either by doping with antimony or by the presence of oxygen deficiencies, exhibits a crossover of 50 to 60 V and a peak yield of 1.9 (Ref. 3). Since this looked like a promising material for use as a high-power cathode, a sputtered  $\text{SnO}_2$  (6-percent Sb) film was subjected to heavy electron bombardment by the ABMDA phased-array radar group in this Laboratory. After bombarding with 1000-eV electrons of sufficient current density to soften the film's glass substrate (indicating a temperature between 700° and 1000°C), the secondary emission properties were measured again. The results are shown in Fig. IV-3. Figure IV-3(a) is a spot in the most heavily bombarded region and hence was subjected to a higher temperature than the spot in Fig. IV-3(b), which was near the edge of the beam. The peak yield is still 1.75, and the crossover voltage is still between 50 and 60 V. Auger spectra of the secondary electrons showed that the material was still  $\text{SnO}_2$ , indicating little degradation of the film even under severe bombardment.

The highest yields, however, are seen in material like  $\text{MgO}$ ,  $\text{BeO}$  and  $\text{Al}_2\text{O}_3$ , none of which can be made partially conducting by bulk doping. The only way that charge can be removed from these materials under DC bombardment is for the oxide to be so thin that charge can tunnel from the surface to some adjacent conducting region. Thin layers of  $\text{BeO}$  on  $\text{BeCu}$  have been used as cathodes in some low-power devices, but the layer will not stand up under electron bombardment. It should be possible, however, to make a bulk emitter utilizing a mixture of insulating and conducting particles where the individual insulating grains are small enough to allow tunneling to the

conducting regions. Since this requires particle sizes less than 100 Å (Ref. 4), powder mixtures are not feasible. We decided to try obtaining a sufficiently small grain size by sputtering a metal-insulator mixture onto a relatively cool substrate.

In order to get a distinct two-phase metal-insulator system, we used a mixture of gold and MgO, the assumption being that gold is sufficiently inert to sputter as pure gold and that MgO is stable enough not to disassociate and form other compounds (or at least that  $Mg^{2+}$  and  $O^{2-}$  ions would recombine as MgO on the substrate). A mixture of 42-percent gold by volume was chosen initially since work on the electrical conductivity in disordered systems has shown that there is almost unity probability of having conducting paths in a conductor-insulator system for more than 40-percent conductor.<sup>5</sup> Samples were grown on quartz substrates at 50, 200 and 350°C by

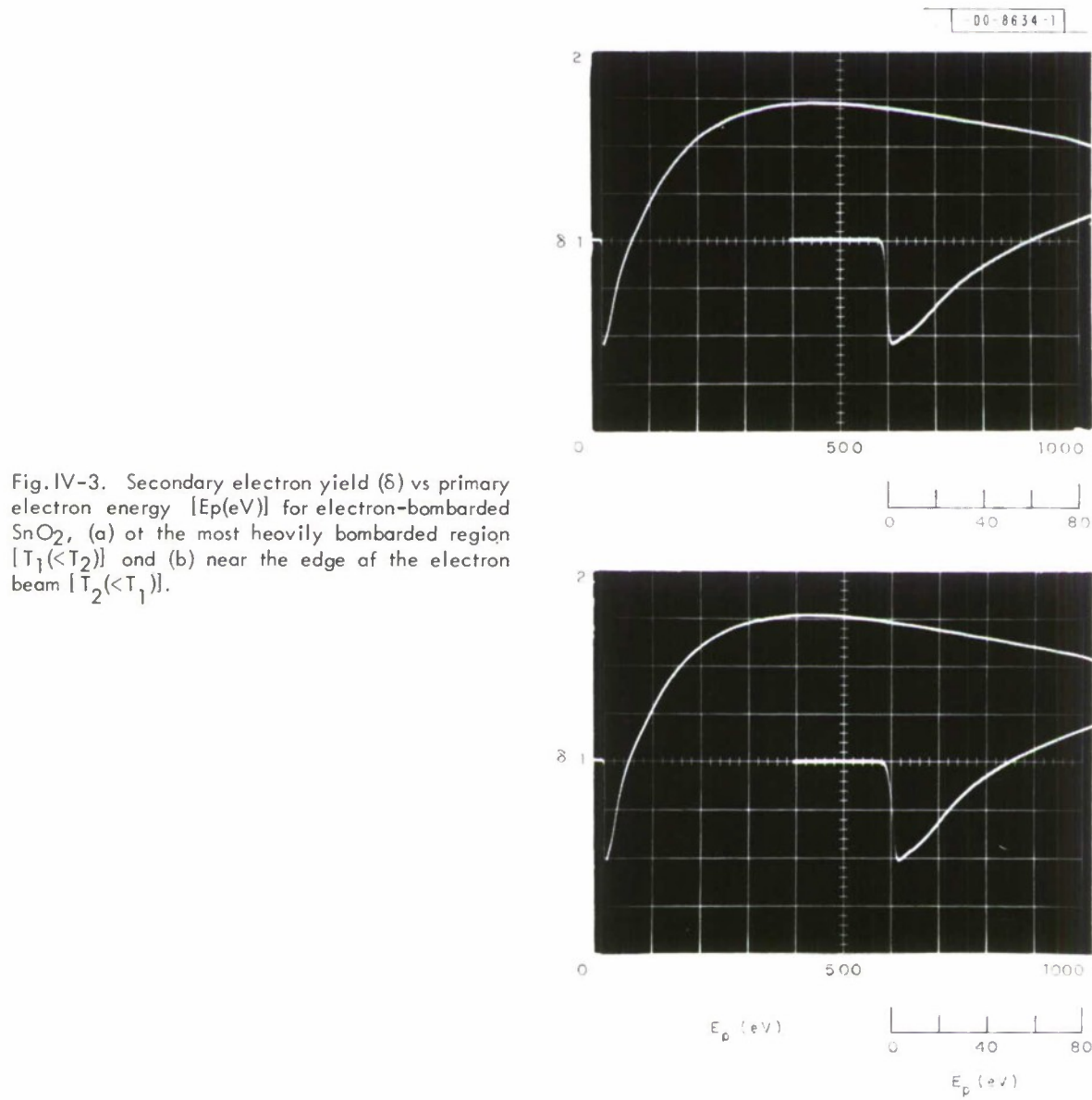


Fig. IV-3. Secondary electron yield ( $\delta$ ) vs primary electron energy [ $E_p$ (eV)] for electron-bombarded  $SnO_2$ , (a) of the most heavily bombarded region [ $T_1 < T_2$ ] and (b) near the edge of the electron beam [ $T_2 < T_1$ ].

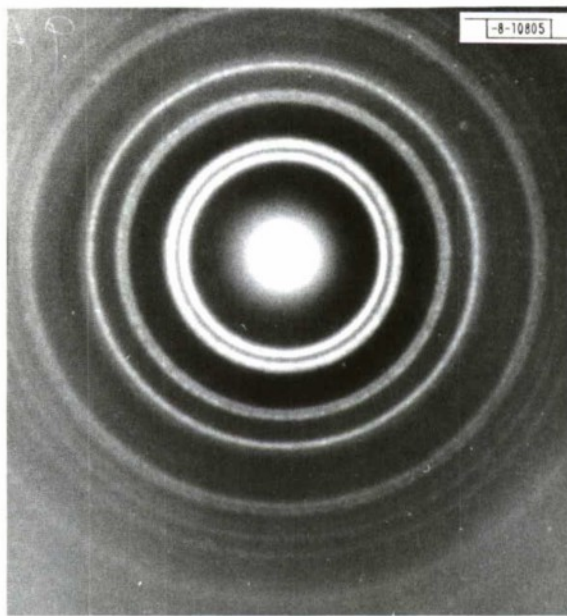


Fig. IV-4. Transmission electron diffraction pattern of a MgO-Au sputtered film on a 200°C substrate.

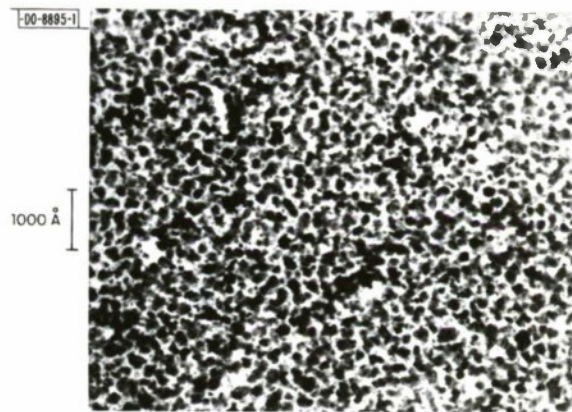


Fig. IV-5. Bright-field electron micrograph of the film used in Fig. IV-4.

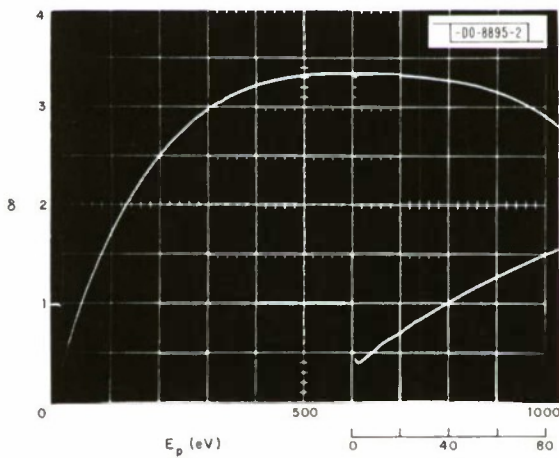


Fig. IV-6. Yield ( $\delta$ ) vs primary electron energy [ $E_p$ (eV)] for a 0.42 + 0.58 MgO film sputtered on a 50°C substrate.

DC sputtering using argon gas. The thickness of the films, measured by thin-film interferometry, was about 380 Å. Film composition was determined by electron diffraction.<sup>†</sup> Reflection patterns using 75-keV electrons showed that all the samples are polycrystalline and have the same diffraction patterns, except that sharper diffraction rings on the 350°C sample indicated larger microcrystalline size than for the other two substrate temperatures. Transmission diffraction patterns were made on the 200°C film using 80-keV electrons (Fig. IV-4). The location of the diffraction rings verifies the existence of a distinct, two-phase system of gold and MgO (Table IV-1). Microcrystallite size was measured by bright-field transmission electron micrography on the 200°C film (Fig. IV-5), showing a maximum grain size of about 200 Å.

The films deposited at 200°C were too highly resistive to allow measurement of the secondary electron yield, but the 50° and 350°C samples had sufficient conductivity that they showed no charging effects. The yield of the 50°C sample, sputtered atomically clean by argon-ion bombardment, is shown in Fig. IV-6. It has a crossover of 40 eV and a peak yield of 3.4. This is to be compared to a crossover of 50 to 60 eV and a peak yield of 1.9 for SnO<sub>2</sub>. (Note the change

TABLE IV-1  
COMPARISON OF LATTICE SPACINGS OF A MgO-Au FILM  
SPUTTERED AT 200°C FROM TRANSMISSION ELECTRON MICROSCOPY  
WITH SPACINGS LISTED IN ASTM INDEX  
(Measurement accuracy  $\pm 1$  percent)

d (Å)	ASTM Index	
	MgO	Au
2.35	—	2.34 (111)
2.10	2.10 (200)	—
1.49	1.49 (220)	—
1.44	—	1.44 (220)
1.23	1.22 (222)	1.23 (311)
1.18	—	1.18 (222)
0.931	—	0.936 (331)
0.909	—	0.912 (420)
0.860	0.860 (422)	—

in yield scale between Fig. IV-3 and Fig. IV-6.) We are currently making detailed studies of the effects of conducting and insulating substrates, substrate temperature, annealing and composition on the yield of Au-MgO films, as well as exploring other metal-insulator systems. We feel that these preliminary results make sputtered metal-insulator films promising candidates for efficient secondary-emitting cathodes.

V. E. Henrich  
J. C. C. Fan

<sup>†</sup> We would like to acknowledge the use of Harvard University facilities for some of the above studies, especially in the electron microscopy studies, where the assistance of Mr. Gail Pierce is greatly appreciated.

## Section IV

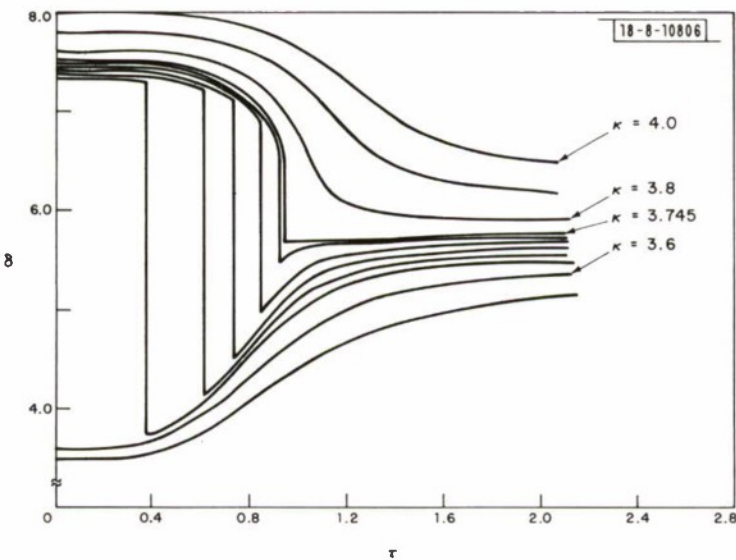


Fig. IV-7. Calculated curves of  $\delta$  vs reduced temperature  $\tau$ , for a series of values of  $\kappa$ . Parameters have been chosen to represent the case of  $V_2O_3$ , with two electrons per cation.

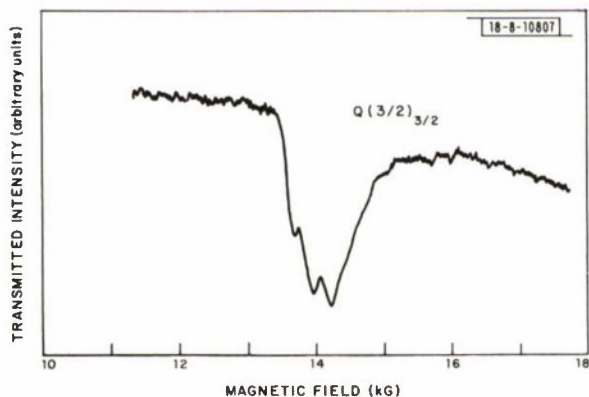


Fig. IV-8. Zeeman spectrum of the  $Q(3/2)_{3/2}$  line of NO taken with a CO laser emitting on the  $P(15)_{9,8}$  line.

### C. APPLICATION OF FREE ENERGY MODEL TO THE HIGH TEMPERATURE PHASE TRANSITION IN Cr-DOPED V<sub>2</sub>O<sub>3</sub>

The free energy model developed for the description of the insulator-metal transition in Ti<sub>2</sub>O<sub>3</sub> (Ref. 6) has been extended to the case of two electrons per cation, corresponding to V<sub>2</sub>O<sub>3</sub>. A series of curves of c-axis parameter vs normalized temperature has been calculated, for different values of  $\kappa$ , which is qualitatively very similar to the series of experimental curves for different values of chromium concentration. The change in value of c-axis parameter in the model is proportional to the number of electrons in band 2, which is proportional to the calculated parameter  $\delta$ . Figure IV-7 shows a series of such curves.

The curve labeled  $\kappa = 3.8$  corresponds to a case where at low temperatures a narrow band (band 1) lies above the Fermi surface in a partially filled, broader band (band 2). As the temperature increases, band 1 drops smoothly below the Fermi surface, with a corresponding decrease in c-axis parameter. For  $\kappa = 3.745$ , the drop of c-axis parameter with increasing temperature is at first smooth, but a first order transition occurs at  $\tau = 0.95$ . The first order transition temperature continues to decrease with decreasing  $\kappa$ , so that by  $\kappa = 3.6$ , band 1 is already below the Fermi surface at T = 0. Thus, for a decrease in  $\kappa$  of ~5 percent, a series of curves is obtained which looks much like the series produced by the addition of a few percent of Cr to V<sub>2</sub>O<sub>3</sub>. A further study of the model for various values of parameters is under way.

H. J. Zeiger

### D. LASER SPECTROSCOPY

#### 1. Zeeman Spectra of Q-Branch Absorption Lines of NO

We have previously studied the Zeeman splitting of R-branch lines in the fundamental ( $v = 0$  to  $v = 1$ ) vibration-rotation band of NO using both fixed frequency CO lasers,<sup>7,8</sup> and tunable semiconductor diode lasers.<sup>9</sup> In these measurements we did not detect any significant deviation from the simple, linear Zeeman effect because the character of the Zeeman spectra for R-branch lines is dominated by the rotational dependence of the energy levels. However, Q-branch transitions involve levels which have the same rotational quantum number J and the splitting of observed transitions is particularly sensitive to the dependence of g on the initial and final state quantum numbers. We have obtained Zeeman spectra of the Q(3/2)<sub>3/2</sub> and Q(5/2)<sub>3/2</sub> absorption lines of NO by tuning these lines into coincidence with the P(15)<sub>9,8</sub> emission line of a CO gas laser. Both of these spectra exhibit fine structure which results from a lifting of degeneracy of the Zeeman transitions due to variation in the g-factor with state quantum number. Furthermore, the line splittings in the observed fine structure are surprisingly large.

Figure IV-8 shows the signal transmitted through a 4-cm-long gas cell (containing 10 torr of NO) as a function of applied magnetic field. The data were taken as described previously<sup>7</sup> using the P(15)<sub>9,8</sub> line of a highly stable CO laser. As expected, there is one major Zeeman line near 14 kG due to the Q(3/2)<sub>3/2</sub> absorption line of NO. However, this line is split into three closely spaced components separated equally by 250 G. Since the transition involved is J = 3/2 to J = 3/2, there are several effects which could yield these three lines: (1) high magnetic field nuclear hyperfine splitting, and (2) vibrational and/or nonlinear Zeeman splitting of the otherwise degenerate Zeeman lines. For a magnetic field of 14 kG, the N<sup>14</sup> nuclear spin is uncoupled from the molecular angular momentum and separately quantized along the field. Under these

#### Section IV

circumstances the hyperfine spectrum should consist of three equally spaced lines having equal intensities and an energy separation of 29 MHz (independent of the magnetic field). For  $J = 3/2$ , the calculated  $g \approx 0.78$  and the field tuning rate for  $Q(3/2)_{3/2}$  is 1.1 MHz/G, yielding a hyperfine line separation of 27 G. This value is nine times smaller than that observed and smaller than the observed linewidths. Thus, the fine structure of Fig. IV-8 is not due to hyperfine coupling.

If  $g$  were independent of the molecular vibrational state, the absorption spectrum of Fig. IV-8 would therefore consist of a single line which had three degenerate components each being an allowed transition with  $\Delta M_J = +1$ . A vibrational dependence of  $g_J(v)$  would split the single line into three equally spaced lines with a separation

$$\Delta B \approx \frac{g_{3/2}^{(1)} - g_{3/2}^{(0)}}{g_{3/2}^{(0)}} \left( \frac{E_0}{\mu_B g_{3/2}^{(0)}} \right) \quad (\text{IV-1})$$

where  $\mu_B$  is the Bohr magneton and  $E_0$  is the zero field separation of the  $P(15)_{9,8}$  CO laser line and the  $Q(3/2)_{3/2}$  NO absorption line. From the known molecular vibration-rotation parameters of CO and NO, one finds  $E_0$  to be  $0.50 \text{ cm}^{-1}$ . We can estimate the vibrational dependence of  $g_J$  using the result of Dousmanis, *et al.*,<sup>10</sup> for  $^2\Pi_{3/2}$  states intermediate to Hund's cases (a) and (b),

$$g_J(v) = \frac{1}{J(J+1)} \left[ \frac{3}{2} - \frac{2(J - \frac{1}{2})(J + \frac{3}{2}) - \frac{3}{2}\lambda_v + 3}{[4(J + \frac{1}{2})^2 + \lambda_v(\lambda_v - 4)]^{1/2}} \right] \quad (\text{IV-2})$$

where  $\lambda_v = (A_v/B_v)$ , and  $A_v$  is the vibration-dependent spin-orbiting splitting of  $^2\Pi_{1/2}$  and  $^2\Pi_{3/2}$  energy levels and  $B_v$  is the vibration-dependent rotational constant. Keck and Hause (Ref. 11) give

$$\begin{aligned} A_0 &= 123.20 \text{ cm}^{-1} & , & \quad A_1 = 122.95 \text{ cm}^{-1} & , \\ B_0 &= 1.696 \text{ cm}^{-1} & , & \quad B_1 = 1.678 \text{ cm}^{-1} & . \end{aligned}$$

Using these values, we calculate from Eq. (IV-2),

$$g_{3/2}^{(0)} = 0.7769$$

and

$$g_{3/2}^{(1)} = 0.7771$$

Then, Eq. (IV-1) yields a line separation  $\Delta B = 3.4 \text{ G}$ . This value is almost two orders of magnitude smaller than the observed separation of 250 G. This discrepancy suggests that the proper explanation for the observed splitting may lie in higher order corrections to the Zeeman energies which are nonlinear in  $B$  and would yield an effective  $g$ -factor which was state dependent. The effect of these nonlinear Zeeman terms would be quite analogous to the effect of a vibrational dependence of  $g$ . It should be noted that (a) only a small difference ( $\approx 1.5$  percent) between  $g_{3/2}^{(1)}$  and  $g_{3/2}^{(0)}$  is required to explain our observations and (b) explaining the data in terms of the nuclear hyperfine coupling would require a very large discrepancy between observed and calculated hyperfine energies, contrary to our previous observations.<sup>12</sup>

The Zeeman spectrum of  $Q(5/2)_{3/2}$  is shown in Fig. IV-9. In this case there are four Zeeman components which are well separated. Hyperfine splitting would give only three lines (independent of the  $J$  value involved). However, five lines are expected for a  $Q(5/2)$  line which is split due to a variation in  $g$  with level quantum number and/or  $B$ . Furthermore, the lines

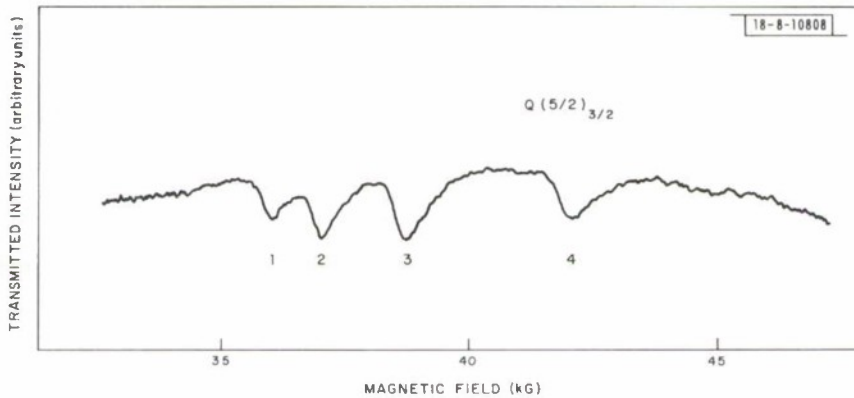


Fig. IV-9. Zeeman spectrum of the  $Q(5/2)_{3/2}$  line of NO taken with a CO laser emitting on the  $P(15)_{9/8}$  line (path length, 4 cm; pressure, 10 torr).

should be about equally spaced. Thus, there appears to be a line missing between lines 3 and 4 of Fig. IV-9. The explanation for this discrepancy concerning the number of lines observed is not immediately apparent. It is interesting to note that the data of Fig. IV-9 indicate that  $g_{5/2}^{(1)}$  is about 4 percent larger than  $g_{5/2}^{(0)}$ , much larger than the 0.07 percent expected based on Eq. (IV-2).

The explanation for the rather large state dependence of  $g_J$  suggested by our data may lie in refinements in the expression for  $g_J$  [Eq. (IV-2)] which would include coupling to the higher lying  $\Sigma$  electronic state and/or the effects of the strong magnetic field on the electronic states. Further quantitative study of these effects is planned.

F. A. Blum  
K. W. Nill

## 2. Observation of Nuclear Hyperfine Structure in the R-Branch of NO at 77°K

Previous high resolution measurements<sup>12</sup> on the  $^2\Pi_{1/2}$  Q-branch of NO at 300°K have revealed structure of the absorption lines due to nuclear hyperfine splitting of the rotational levels. This structure is particularly large in the Q-branch since the splitting of these vibration-rotation transitions is proportional to the sum of the nuclear hyperfine splittings of the  $v = 0$  and  $v = 1$  rotational levels. The electric dipole selection rules for the R-branch vibration-rotation transitions result in hyperfine splittings proportional to the differences of the splittings of the rotational levels involved. Consequently, it is quite difficult to observe features of these absorption lines due to nuclear hyperfine coupling because of the obscuring effects of the Doppler broadening (129 MHz). Since the Doppler width is proportional to  $T^{1/2}$ , reducing the gas temperature to 77°K from room temperature results in a Doppler width of only 65 MHz. While NO freezes below 109.3°K, the vapor pressure above the solid<sup>13</sup> is about 1 torr at 77°K and for the lines studied ~80 percent absorption was obtained in a 5-cm, 77°K gas cell. A comparison of the transmission

## Section IV

of the gas cell near  $R(3/2)_{1/2}$  and  $R(3/2)_{3/2}$  at 295° and 77°K is shown in Fig. IV-10. The transmission data of Fig. IV-10(a) were taken at room temperature with 4 torr of NO and the 129-MHz Doppler absorption width is apparent. At this pressure there is also a slight (~5 MHz) increase of the linewidth due to pressure broadening (4.6 MHz/torr). The two components of  $R(3/2)_{1/2}$  result from  $\Lambda$  doubling<sup>9</sup> and are separated by 350 MHz. The  $R(3/2)_{3/2}$  absorption is a single line whose integrated absorption strength is less than  $R(3/2)_{1/2}$  due to the lower population of the  $^2\Pi_{3/2}$  state relative to the  $^2\Pi_{1/2}$  state at room temperature. The  $^2\Pi_{3/2}$  state lies above the  $^2\Pi_{1/2}$  state by the spin-orbit splitting of  $123\text{ cm}^{-1}$  and its thermal population at room temperature ( $kT \sim 200\text{ cm}^{-1}$ ) is only about 1/3 of the  $^2\Pi_{1/2}$  state. Figure IV-10(b) illustrates the effect of lowering the gas temperature to 77°K; the Doppler width is considerably reduced and the  $R(3/2)_{3/2}$  line is much weaker relative to  $R(3/2)_{1/2}$  since the spin-orbit splitting of the  $^2\Pi_{1/2}$  and  $^2\Pi_{3/2}$  states is now about 2.3 kT. There is a small shoulder on one of the components of  $R(3/2)_{3/2}$  which results from nuclear hyperfine coupling. Structure due to nuclear hyperfine coupling is more apparent in the  $R(1/2)_{1/2}$  transmission spectra shown in Fig. IV-11. The room temperature transmission of  $R(1/2)_{1/2}$  in Fig. IV-11(a) consists of two main components resulting from  $\Lambda$  doubling which are separated by 351 MHz and the only observable effect of nuclear hyperfine coupling is a slight distortion of these components. In the low temperature (77°K) transmission spectrum [Fig. IV-11(b)] the structure produced by nuclear hyperfine splitting of the rotational levels

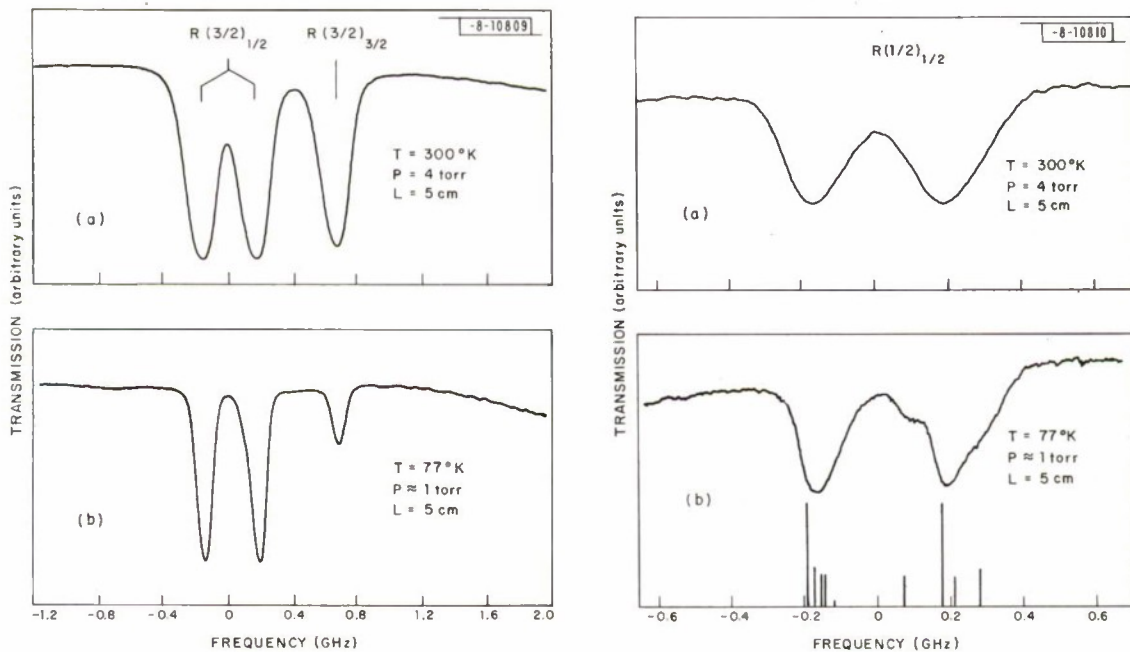


Fig. IV-10. Comparison of the transmission spectrum of NO near  $R(3/2)_{3/2}$  and  $R(3/2)_{1/2}$  for gas temperature of: (a) 295°K and (b) 77°K.

Fig. IV-11. Comparison of the transmission spectrum of NO near the  $R(1/2)_{1/2}$  absorption at  $1881.06\text{ cm}^{-1}$  for gas temperatures of: (a) 295°K and (b) 77°K. The bars indicate the location and strengths of the calculated hyperfine components.

is more apparent. The vertical bars indicate the locations and relative strengths of the calculated hyperfine components of  $R(1/2)_{1/2}$ . There are ten components resulting from transitions between the  $v = 0$ ,  $J = 1/2$  and  $v = 1$ ,  $J = 3/2$  rotational levels. Nuclear hyperfine coupling splits the  $J = 1/2$  levels into two components and the  $J \geq 3/2$  levels into three components. Hence there are only ten hyperfine components for  $R(1/2)_{1/2}$  whereas all other R-branch absorptions have 14 components. Structure due to nuclear hyperfine coupling has not been observed in  $^2\Pi_{3/2}$  transitions since the coupling parameters are quite small in this state.

K. W. Nill  
F. A. Blum  
A. J. Strauss

## REFERENCES

1. Solid State Research Report, Lincoln Laboratory, M.I.T. (1972:3), DDC AD-752556.
2. S.J. Sealise and R.B. Allen, "GaAsP Diode Pumped Nd:YAG Laser," Technical Report AFAL-TR-71-153, Wright-Patterson AFB (1971).
3. Ref. 1, p.55
4. K.A. Pickar, Bell Laboratories Technical Memorandum MM68-2322-1 (1968).
5. D. Adler, L.P. Flora and S.D. Senturia, Solid State Commun. (to be published).
6. H.J. Zeiger, T.A. Kaplan and P.M. Raccah, Phys. Rev. Letters 26, 1328 (1971), DDC AD-729576.
7. Solid State Research Report, Lincoln Laboratory, M.I.T. (1972:2), p.41, DDC AD-748836.
8. See, also, A. Kaldor, W.B. Olsen and A. Maki, Science 176, 508 (1972).
9. K.W. Nill, F.A. Blum, A.R. Calawa and T.C. Harman, Chem. Phys. Letters 14, 234 (1972), DDC AD-752963.
10. G.C. Dousmanis, T.M. Sanders and C.H. Townes, Phys. Rev. 100, 1735 (1955).
11. D.B. Keek and C.D. Hausc, J. Mol. Spectry. 26, 163 (1968); J. Chem. Phys. 49, 3458 (1968).
12. F.A. Blum, K.W. Nill, A.R. Calawa and T.C. Harman, Chem. Phys. Letters 15, 144 (1972), DDC AD-753369.
13. Handbook of Chemistry and Physics, 48 Edition, R.C. Weast, Ed. (Chemical Rubber Publishing Co., 1967), p. D-141.

## V. MICROELECTRONICS

### A. ELECTRON-BEAM SEMICONDUCTOR DIODES

Efforts on the Electron-Beam Semiconductor (EBS) diodes have been directed toward improving the electrical characteristics and measuring the thermal resistance of the devices. The EBS diode is basically a planar  $p^+ - n^- - n^+$  or  $n^+ - p^- - p^+$  junction in which the uppermost region is a very shallow diffused  $p^+$  or  $n^+$  layer. With the diode in reverse bias, an electron beam penetrates the shallow diffused layer creating electron-hole pairs in the (depleted)  $n^-$  or  $p^-$  layer. The beam electrons lose energy in penetrating the diffused layer, and thus the gain, or number of electron-hole pairs generated per incident electron, is a function of the diffusion depth. The gain vs electron beam energy has been measured by W. E. Krag on a number of diodes fabricated for the Electronic Countermeasures Group. We have measured the diffusion depth by standard sectioning techniques. A comparison between the gain at a beam energy of 12 kV and diffusion depth is shown in Fig. V-1. As expected, the gain is largest when the diffused layer is made as thin as possible. However, RF currents will flow through this layer, and it must therefore have a low sheet resistance to minimize RF losses. As the diffused layer is made thinner, this sheet resistance increases. Currently, we are able to produce 4000- $\text{\AA}$  diffused boron layers having a sheet resistance of about 25 ohms per square. Should it become necessary to obtain a lower figure, one would have to consider adding a thin layer of metal over the diode. In one such experiment, 900  $\text{\AA}$  of aluminum was evaporated over a 4000  $\text{\AA}$  shallow  $p^+$  layer. The sheet resistance of the aluminum was approximately 0.4 ohms per square, which is well within the limits posed by RF losses. The addition of aluminum produced an 11-percent drop in gain (Fig. V-1). The next logical step is to eliminate the shallow diffused junction altogether and use a thin layer of metal to form a Schottky-barrier diode. Here the choice of metal must be made carefully so as to be compatible with silicon. Chromium, nickel and molybdenum appear to be promising, while aluminum will not be used on the grounds of metallurgical incompatibility with gold (see below) at elevated temperatures and the possibility of electromigration.

Metalization of the EBS diode has been carefully considered during the past quarter with the goal of finding a system which is compatible with silicon at elevated temperatures. Presently,

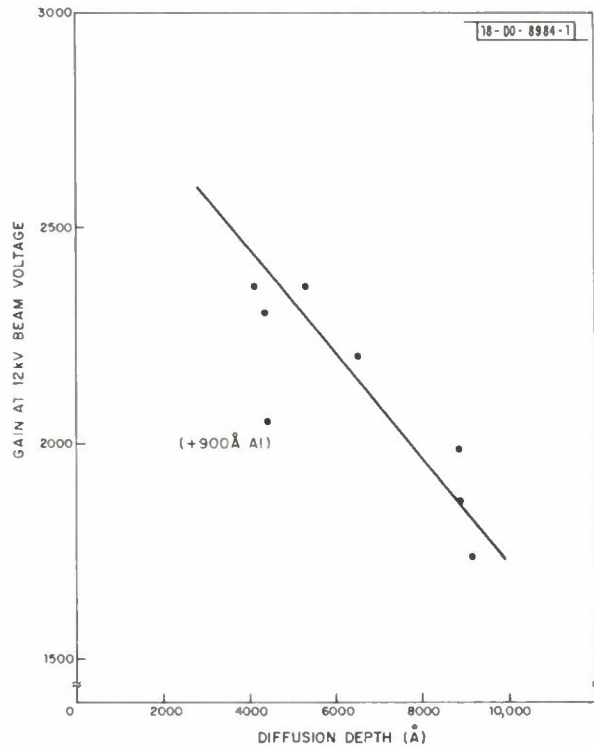


Fig. V-1. Gain reduction due to penetration loss in shallow diffused layer.

## Section V

ohmic contact is made by a ring of evaporated aluminum at the periphery of the diode and a gold shield in turn is bonded to the aluminum. At elevated temperatures ( $>200^{\circ}\text{C}$ ), such a bond can be expected to fail due to purple plague. For this reason an alternative to aluminum is needed. A system developed at Texas Instruments using molybdenum and gold has been shown to be reliable.<sup>1</sup> As a preliminary to making devices using Mo/Au, we have begun experiments to determine (1) if the molybdenum/silicon ohmic contact has sufficiently low resistance, and (2) if the molybdenum is a barrier to the diffusion of gold into the silicon.

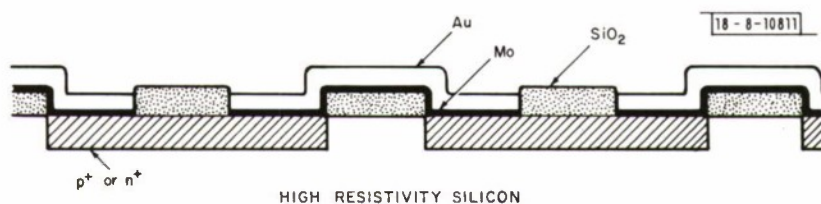


Fig. V-2. Test vehicle for measuring Mo-Si contact resistance.

Contact resistance to  $n^+$  and  $p^+$  silicon has been measured using the system shown in Fig. V-2. The current path goes through a series of Mo-Si contacts, and the contact resistance is calculated from a measurement of the total resistance minus the resistance through the diffused layer under the oxide. The goal was to achieve a specific contact resistance of less than  $5 \times 10^{-3}$  ohm-cm $^2$ , which would result in a 1-ohm contact resistance in the EBS diode. Measured specific resistances on  $p^+$  and  $n^+$  diffused layers in silicon have been less than  $2 \times 10^{-3}$  and  $3 \times 10^{-4}$  ohm-cm $^2$ , respectively. The doping levels at the surface were approximately  $10^{20}$  and  $10^{21}$  cm $^{-3}$ , respectively. The Mo-Au films were E-gun evaporated onto substrates heated to  $250^{\circ}\text{C}$ . Further details on these experiments can be found in Sec. V-C.

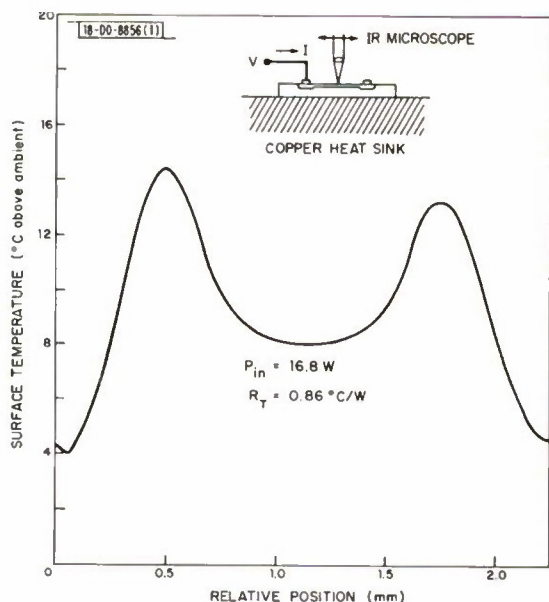


Fig. V-3. Thermal profile of EBS diode.

Measurements of the thermal resistance of EBS diodes are difficult to interpret using conventional methods. The usual techniques for diodes involve either forward or reverse (into breakdown) bias to generate heat in the diode and the measurement of some temperature sensitive parameter of the diode, such as forward resistance. If the current flow is not uniformly distributed over the junction, the temperature rise will also not be uniform and the results cannot be easily interpreted. In the case of the EBS, the forward-bias current flow is confined to the diffused guard ring under the metalization. The situation requires detailed knowledge of the temperature variation over the area of the diode. In Fig. V-3 we show the results of a measurement of the surface temperature taken across the diameter of an EBS diode. The surface was covered with

lampblack to bring the emissivity close to one and the temperature measured by an infrared microscope employing a cooled InSb detector. As expected, the heat generated by forward biasing of the diode is at maximum under the contact metalization ring. The thermal resistance in this case was  $0.86^{\circ}\text{C/W}$ . From this data one can estimate the thermal resistance for the case of uniform current flow, which more closely approximates the operation of the device under an E-beam. Such an estimate lies below  $2^{\circ}\text{C/W}$ , which has been the design goal.

Progress has been made toward increasing the breakdown voltage of the EBS diode. This has been an important goal, because the diode efficiency increases with reverse bias, but this bias must be kept below avalanche breakdown. The maximum theoretical breakdown voltage has seldom been achieved until now, with  $p^+/n$  devices showing consistently lower breakdown voltages than the  $n^+/p$ . For these reasons and the fact that the  $p^+/n$  configuration is more desirable in EBS applications, we have performed experiments on the  $p^+/n$  structures shown in Fig. V-4 in order to understand the causes of premature breakdown.

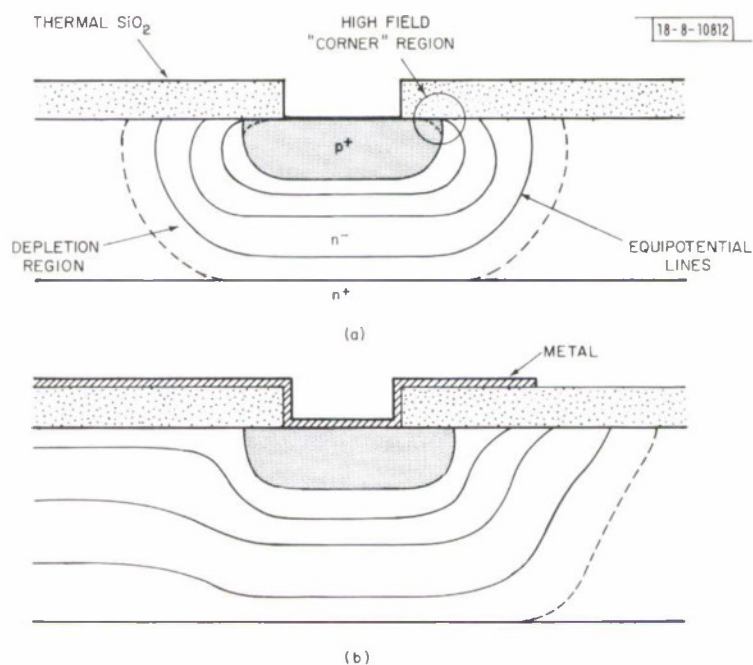


Fig. V-4. Diode structures for use in breakdown voltage studies. (a) Without shield. (b) With metal junction shield.

The investigation into this problem has been aided considerably by use of the laser scanner.<sup>2</sup> Briefly, a focused beam of light ( $\lambda = 6328 \text{ \AA}$ ) from a He-Ne laser scans the surface of a reverse-biased diode. The light generates electron-hole pairs, and the resulting photocurrent from the device is amplified and used to modulate the intensity of a TV picture. The TV frame is scanned in synchronism with the laser so that "pictures" of devices can be made, often revealing information not evident from a visual inspection or readily obtained by other means. Examples of the laser scanner pictures of the devices shown in Fig. V-4 are found in Fig. V-5. Interpretation of these pictures can be made by reference to the structure of the diodes shown in Fig. V-4. The diode is the basic EBS structure consisting of a circular 4- $\mu\text{m}$ -deep  $p^+$  (boron) guard ring diffusion

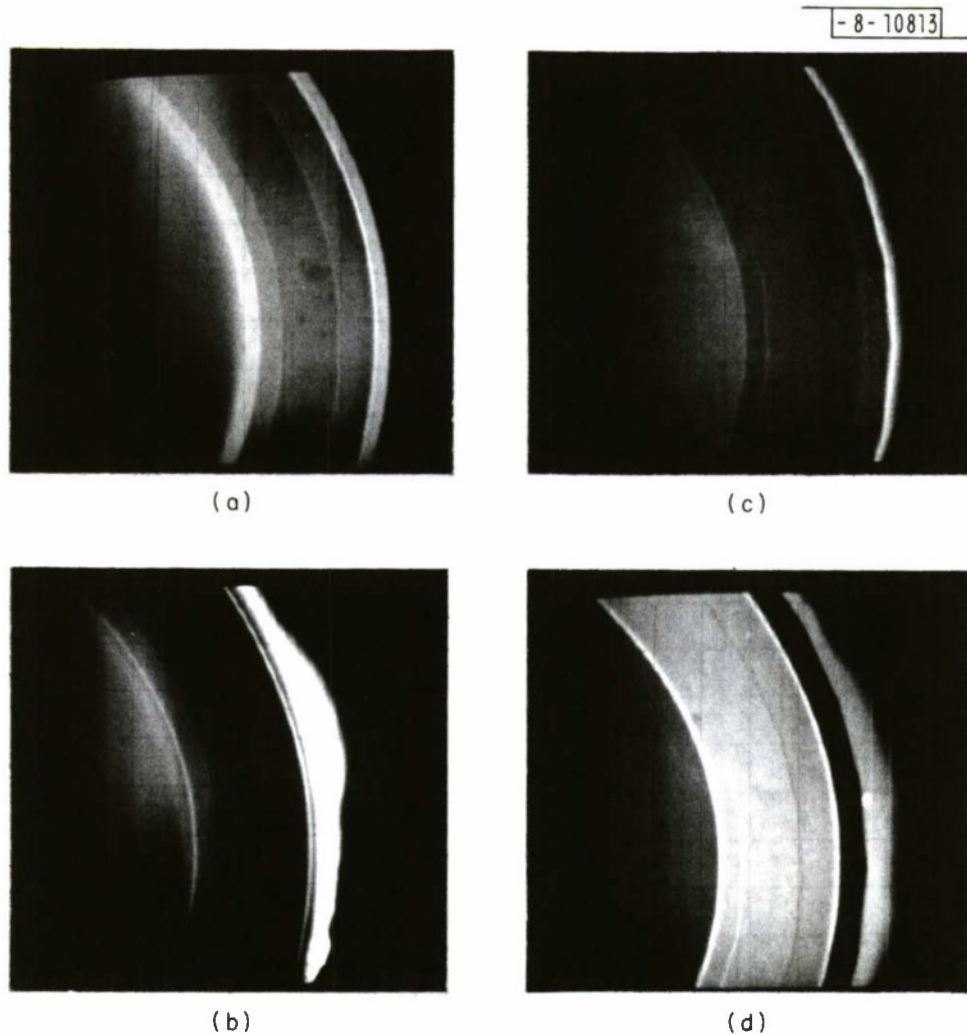


Fig. V-5. Laser scanner photographs of diodes in Fig. V-4 under reverse bias. Diode without shield [Fig. V-4(a)] is shown in (a) and (b) under bias of 150 and 190 V, respectively. Diode with junction shield [Fig. V-4(b)] is shown in (c) and (d) under bias of 150 and 240 V, respectively.

into an  $n/n^+$  epitaxial wafer but without the usual shallow  $p^+$  diffusion. Under reverse bias, a depletion region is formed extending to the sides and down to the  $n^+$  substrate. Carriers generated in the depletion region are swept out, while those generated in the neutral regions outside the depletion region remain stationary and do not contribute to the current. In Fig. V-5(a) [corresponding to the device of Fig. V-4(a)] the depletion region at the inner and outer edges of the guard ring can be seen as the two brightest rings, while the guard ring is represented by the darker bands in between. The  $p^+$  region is darker because the laser light must penetrate 4  $\mu\text{m}$  of silicon to reach the depletion region. The photograph was taken with the diode biased to 150 V, although the picture is essentially the same at biases down to a few volts. At a bias of 190 V bright regions begin to appear at the edge of the guard ring as seen in Fig. V-5(b). (In this photo the laser intensity was turned down to emphasize the "brightness" of these regions.) In this case, the electric field intensity has increased to the point where the photo-generated carriers are now creating other electron-hole pairs via impact ionization. This current multiplication registers as a bright region on the display and is a valuable means for determining where avalanche breakdown is occurring. This mode of breakdown at the guard ring edge is a common feature of  $p^+/n$  diodes and is believed to be the result of a sharp curvature in the  $p^+/n^-$  junction at the surface [dashed line in the encircled area of Fig. V-4(a)]. It is well known that because of the higher field intensity a curved junction has a lower breakdown voltage than a plane junction. The junction curvature may be the result of either the fixed positive charge always found in thermal  $\text{SiO}_2$  or of the fact that the  $\text{SiO}_2$  is known to leach boron out of the silicon at high temperatures causing the concentration of boron under the oxide to be reduced. Both of these hypotheses are consistent with the observation that  $n^+/p$  diodes have higher breakdown voltages; unlike boron, the phosphorus (in an  $n^+$  guard ring) concentration is not depleted at the  $\text{Si}/\text{SiO}_2$  interface.

A remedy to this problem has been suggested by the work of Grove, *et al.*,<sup>3</sup> as well as others, who have studied the effect of placing electrodes ("gates") over the junction and biasing them independently of the junction. Such structures are called gate-controlled diodes. It has been shown that the breakdown voltage of such diodes could be varied over a wide range by using the gate electrode to modify the field structure near the junction. In the case of the EBS diode, the extra, independently biased electrode would complicate the device, and it was felt that nearly as good results could be achieved with a single electrode, as shown in Fig. V-4(b). The effect of the metal shield is to push the equipotential lines away from the point where the junction meets the surface and thus away from the region where breakdown was known to occur.

A graphic illustration of the efficacy of this electrode is shown in the laser scans of Figs. V-5(c) and (d). The metal junction shield consists of an evaporated film of chromium sufficiently thin to allow partial penetration of the laser. In Fig. V-5(c) the diode is biased to 150 V and part of the depletion edge beyond the junction shield is seen as a bright ring. Next to it is a darker band which is that part of the depletion layer under the Cr, followed by three bands corresponding to the guard ring. With the metal shield, the diode could be biased to nearly 250 V before the avalanche current became excessive. Figure V-5(d), at 240 V, shows that the edge breakdown has been suppressed and instead the breakdown is now occurring uniformly between the guard ring and the  $n^+$  substrate. A small bright spot at the edge of the Cr can also be seen indicating localized breakdown at a defect. The breakdown is now at the theoretical maximum

## Section V

for this structure, and any further increase in breakdown voltage would require a thicker n<sup>-</sup> epitaxial layer. Results on numerous other diodes on the test wafer have shown that the metal shield consistently raises the breakdown voltage by 20 to 25 percent.

B. E. Burke  
R. A. Cohen

### B. IMPATT DIODE PACKAGING FACILITY

The K<sub>a</sub>-band GaAs IMPATT diodes, described in an earlier report by R. A. Murphy, *et al.*,<sup>4</sup> require special packaging and assembly techniques to optimize the microwave performance of the devices. These diodes will be incorporated in the RF amplifier of the transmitter of the LES-8 and -9 satellites.

A packaging facility is being set up in the Microelectronics Group to provide for these procedures. A process flow chart of the procedures and the essential documentation has been drafted and a new technician is being trained for the program.

Equipment is being procured for the gold-tin soldering of the package elements to the strict dimensional tolerances required, as well as for the thermal compression bonding of the gold ribbon contact to the 2-mil-diameter junction. Provisions are being made to monitor the diode characteristics and capacitance during assembly. Hermeticity of the completed package will be evaluated with a helium mass spectrometer.

An exhaust hood is being installed and the hot stage, which permits soldering procedures to be done in a controlled atmosphere, is now in operation in a temporary location. Additional facilities will be activated as the equipment becomes available.

T. F. Clough

### C. USE OF MOLYBDENUM AND MOLYBDENUM-GOLD FILMS AS METALIZATION FOR SILICON DEVICES

Although aluminum has many attractive characteristics as a metalization system for use with silicon devices (low resistivity  $2.6 \times 10^{-6}$  ohm-cm, ease of deposition and patterning, good adhesion to silicon and silicon dioxide, and ohmic contact to silicon in most circumstances), there are certain problems with aluminum that make its use unacceptable in certain applications. First, aluminum alloys with silicon which may result in the shorting of shallow junction devices. Second, aluminum is susceptible to electromigration damage in the form of voids, hillocks and opens. Opens are an obvious problem. However, hillocks can result in shorting between levels in devices requiring multilevel metalization, and voids can markedly increase the effective resistivity of the aluminum.

For both shallow junction devices and multilevel metalization systems, the possibility of using a low resistivity, refractory metal, such as molybdenum ( $5.3 \times 10^{-6}$  ohm-cm), either alone or in combination with gold (to replace aluminum) is very attractive. Molybdenum is resistant to electromigration damage and does not alloy with silicon or gold. Molybdenum also adheres well to both silicon and silicon dioxide and forms ohmic contacts to n- or p-type silicon if a light HF dip is used prior to deposition. Currently, two methods for depositing molybdenum both singly and in combination with gold are under investigation.

In order to evaluate molybdenum as the interconnects in a multilevel metalization system, 5000-Å-thick molybdenum films have been sputtered onto silicon substrates. The depositions

were done both with the substrates heated to approximately 600°C and with the substrates unheated but insulated from the substrate holder with a 0.032-inch-thick piece of borosilicate glass, which allowed the substrate to reach an elevated equilibrium temperature as the result of electron bombardment. In the latter case, resistivities of  $14 \times 10^{-6}$  ohm-cm were achieved. The heated substrates yielded molybdenum films with close to bulk resistivity. Films deposited using both techniques etched easily using normal photolithographic techniques and had excellent adherence to silicon. Although a further reduction in the effective bulk resistivity of the molybdenum films is desirable, the resistivities already demonstrated make molybdenum an attractive replacement for aluminum, whose resistivity can degrade considerably due to void formation. In addition, the fact that molybdenum does not form hillocks precludes the possibility of isolation dielectric penetration and interlevel shorts between metalization layers.

A second application of molybdenum is in molybdenum/gold composite films deposited with an electron-beam heated source onto silicon substrates heated to 250°C. This composite metallization is intended to provide a system that will not degrade in resistivity after prolonged operation at elevated temperatures. The more commonly used systems (titanium/gold and chromium/gold) degrade very rapidly due to the high metallurgical reactivity of gold with both titanium and chromium. However, molybdenum is metallurgically inert with both gold and silicon.

When used in combination with gold, the molybdenum must perform two functions. First, molybdenum must provide an adhesive layer between the gold and silicon and silicon dioxide. As discussed above, molybdenum does adhere well to these surfaces, and the adherence of the gold to the molybdenum is not a problem when they are evaporated sequentially in the same pump-down. The second function of molybdenum is to provide a barrier layer between gold and silicon to prevent the formation of a gold/silicon eutectic which would destroy the junction under the molybdenum/gold contact. Molybdenum/gold films with 500, 1000 and 2000 Å of molybdenum have been tried. Initial experiments indicate that all three thicknesses yield pinhole-free films which will satisfy both requirements. However, a problem arises in photolithography. If gold overhangs the underlying molybdenum film, at elevated temperatures the gold will migrate down and react with the silicon beneath. The effect is independent of the molybdenum film thickness, but can be controlled by using a double masking procedure to etch the gold and the molybdenum in a way that will insure a rim of molybdenum extending beyond the boundaries of the gold.

F. J. Bachner  
R. A. Cohen  
B. E. Burke

#### D. THIN-FILM INDUCTORS

Spiral inductors have been designed, fabricated and tested with excellent agreement between actual and predicted performance. Equations derived previously<sup>5</sup> were used to design a pair of concentric inductors of 32 µH each. A special computer program was written to generate the mask for these inductors, and conventional photo-engraving techniques were used to fabricate the inductors on a flexible plastic substrate (Kapton). Both inductors had electrical characteristics equivalent to conventional inductors wound with 30-gauge copper wire.

W. H. McGonagle  
D. L. Smythe, Jr.

## Section V

### E. THIN-FILM RESISTOR CHIPS

We have recently worked out a cooperative arrangement with a vendor who fabricates custom, thin-film resistors on silicon substrates for use in hybrid circuits. Two custom networks were designed here, and masks were shipped to the vendor, who in turn used the masks to manufacture the resistor networks to our specifications. One of these networks contained six resistors with a total resistance of 470 kohms on a  $0.030 \times 0.030$  inch chip. These devices were found to be quite satisfactory in every respect and require much less area than the individual thick-film resistors used previously.

D. L. Smythe, Jr.

### F. LAYOUT AND MASK MAKING AREAS

The layouts for several new devices were completed, including spiral inductors, thin-film resistor chips, a charge-coupled imaging device and an infrared television target simulator. These masks, combined with work for other groups, resulted in the delivery of 280 finished masks during the past three-month period. Approximately 20 percent of these masks were chrome.

D. L. Smythe, Jr.

### REFERENCES

1. J. A. Cunningham and J. G. Harper, *Electronic Engineer*, 74 (January 1967).
2. R. E. McMahon, *Electronics*, 92 (12 April 1971).
3. A. S. Grove, P. Leistikko and W. W. Hooper, *IEEE Trans. Electron. Devices* ED-14, 157 (1967).
4. Solid State Research, *Lincoln Laboratory*, M. I. T. (1972:2), p. 5, DDC AD-748836.
5. F. S. Burkett, "Improved Designs for Thin Film Inductors," *Proc. Electronics Components Conference*, pp. 184-194 (10-12 October 1972).

UNCLASSIFIED

Security Classification

**DOCUMENT CONTROL DATA - R&D**

(Security classification of title, body of abstract and indexing annotation must be entered when the overall report is classified)